UNCLASSIFIED

AD NUMBER
AD871821
LIMITATION CHANGES

TO:

Approved for public release; distribution is unlimited.

FROM:

Distribution authorized to U.S. Gov't. agencies and their contractors; Administrative/Operational Use; MAY 1970. Other requests shall be referred to David W Taylor Naval Ship Research and Development Center, Bethesda, MD.

AUTHORITY
USNSRDC Notice 10 Aug 1984

THIS PAGE IS UNCLASSIFIED

AD _82 821_

AUTHORITY:

USNSRDC

Notice 10 AUG 84

INVESTIGATION OF ELASTIC STABILITY OF CIRCULAR TOROIDAL SHELLS UNDER UNIFORM EXTERNAL PRESSURE

AD871821

NAVAL SHIP RESEARCH AND DEVELOPMENT CENTER
WASHINGTON, D.C. 20034

INVESTIGATION OF ELASTIC STABILITY OF CIRCULAR

TOROIDAL SHELLS UNDER UNIFORM EXTERNAL PRESSURE

by

Ely G. Fishlowitz

D D C

DEPARTMENT OF STRUCTURAL MECHANICS

RESEARCH AND DEVELOPMENT REPORT

May 1970

Report 3338

MAJOR NSRDC ORGANIZATIONAL COMPONENTS

NSRDC
CARDEROCK
COMMANDER
TECHNICAL DIRECTOR

* REPORT ORIGINATOR

SYSTEMS DEVELOPMENT OFFICE
OH01

SHIP CONCEPT RESEARCH OFFICE
OH70

DEVELOPMENT PROJECT OFFICES
OH20, 50, 80, 90

NSRDL
ANNAPOLIS
COMMANDING OFFICER
TECHNICAL DIRECTOR

NSRDL
PANAMA CITY
COMMANDING OFFICER
TECHNICAL DIRECTOR

DEPARTMENT OF ELECTRICAL ENGINEERING
A600

DEPARTMENT OF MACHINERY TECHNOLOGY
A700

DEPARTMENT OF MATERIALS TECHNOLOGY
A800

DEPARTMENT OF APPLIED SCIENCE
A900

DEPARTMENT OF HYDROMECHANICS
500

DEPARTMENT OF AERODYNAMICS
600

* DEPARTMENT OF STRUCTURAL MECHANICS
700

DEPARTMENT OF APPLIED MATHEMATICS
800

DEPARTMENT OF ACOUSTICS AND VIBRATION
900

DEPARTMENT OF OCEAN TECHNOLOGY
P710

DEPARTMENT OF MINE COUNTERMEASURES
P720

DEPARTMENT OF AIRBORNE MINE COUNTERMEASURES
P730

DEPARTMENT OF INSHORE WARFARE AND TORPEDO DEFENSE
P740

DEPARTMENT OF THE NAVY

NAVAL SHIP RESEARCH AND DEVELOPMENT CENTER

WASHINGTON, D.C. 20034

INVESTIGATION OF ELASTIC STABILITY OF CIRCULAR

TOROIDAL SHELLS UNDER UNIFORM EXTERNAL PRESSURE

by

Ely G. Fishlowitz

May 1970   Report 3338

TABLE OF CONTENTS

LIST OF FIGURES

ii

LIST OF TABLES

NOTATION

a   Midsurface meridional radius

b   Distance between center of the circular meridian and the axis of revolution

E   Young's modulus of elasticity

h   Shell thickness

n   Number of circumferential waves in buckling pattern

p   Uniform external pressure

u   Midsurface meridional shell displacement

v   Midsurface circumferential shell displacement

w   Midsurface radial shell displacement

θ Circumferential angle

ϕ Meridional angle

σ_θ Circumferential stress

σ_ϕ Meridional stress

ν Poisson's ratio

ABSTRACT

A series of eight plastic toroidal shell models of circular
cross section covering a wide geometric range were designed,
built, and tested under uniform external pressure. The results
were compared to collapse pressure predictions of two analyses.
One analysis agreed with experimental collapse pressure to with-
in 10 percent for all but two of the models. The other analysis
agreed with half the models tested to within 10 percent but
seems to be too optimistic for certain geometries. Experimental
strains were recorded and photographs were taken of the models
undergoing deformation during testing. The test results and
analytical predictions indicated that complete toroidal shells
under uniform external pressure appear to be insensitive to
imperfections.

ADMINISTRATIVE INFORMATION

INTRODUCTION

The lack of sufficient experimental verification of theory for the
toroidal shell under external pressure has precluded the serious con-
sideration of this configuration for use as pressure hulls and storage
tanks for undersea applications. This study is part of the effort to ex-
plore novel concepts for undersea pressure-resistant structures to achieve
increased structural efficiency.

In the field of buckling of thin shells, the toroidal shell has
received little attention compared to the cylinder, sphere, and cone.
Koiter[1] describes Machnig's paper on torus stability under uniform external
pressure as a significant first step in the solution of the torus buckling

---

[1]References are listed on page 52.

1

problem. More recently, Jordan[2] has performed a stability analysis on a torus under uniform pressure and axial loads. At about the same time, Sobel and Flügge[3,4] developed a stability analysis for the toroidal shell under uniform external pressure and included test results of four models in a very narrow range of geometries which were in good agreement ($\pm$10 percent) with the analysis. Also, Bushnell[5,6] has developed a general analysis for any shell of revolution which is applicable to the toroidal shell.

The primary objective of this investigation was the experimental verification of analytical predictions of elastic buckling pressures for toroidal shells under uniform external pressure. The experimental models covered a wide range of geometries. Two analyses were used to give analytical predictions--the Sobel and Flügge analysis and the Bushnell analysis. In both analyses, a linear membrane prebuckling solution is used (although the Bushnell analysis has the capability of a nonlinear prebuckling solution). In the analysis of Sobel and Flügge, stability equations for a torus are solved by Fourier series representations of the displacement components developed during buckling to calculate buckling pressure. Bushnell's analysis solves the buckling problem with an energy method and the finite difference technique. Both analyses are described in more detail in the appendix to this report. For the experimental models of this study, buckling pressure calculations using Bushnell's analysis were performed at the Naval Ship Research and Development Center (NSRDC) using a computer program written by D. Bushnell. Calculations by the analysis of Sobel and Flügge were performed by L.H. Sohel with a computer program at Lockheed Missiles and Space Company, Palo Alto, California. In addition to the buckling pressure, the buckling mode was also determined analytically for each experimental model. The mode prediction consists of determining the number of circumferential (θ-direction in Figure 1) waves and whether deformations are symmetric or antimetric about meridional (ϕ-direction) diameter A-A shown in Figure 1. Some examples of symmetric and antimetric deformations are shown in Figure 2.

In addition to the primary objective, there are two secondary objectives: the use of measured strains and photographs to experimentally determine the buckling modes, and the comparison of measured experimental strains to calculated membrane strains.

2
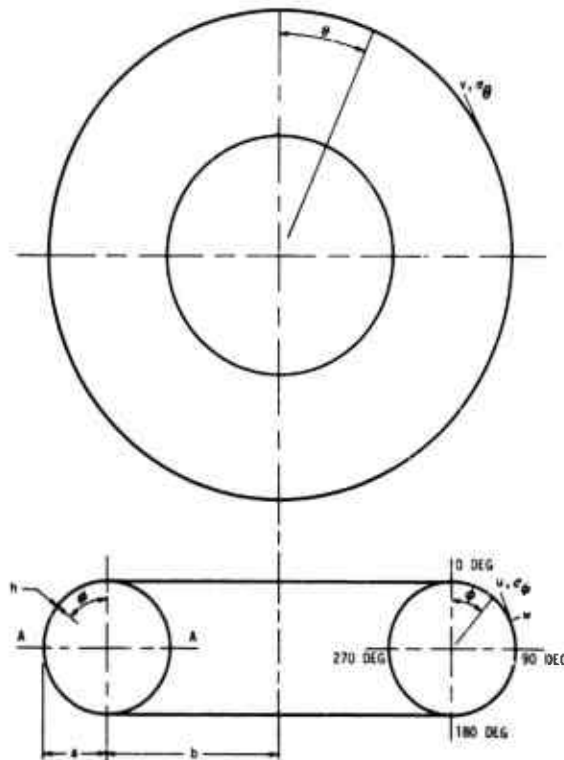
Figure 1 - Toroid Geometry, Displacements, and Stresses
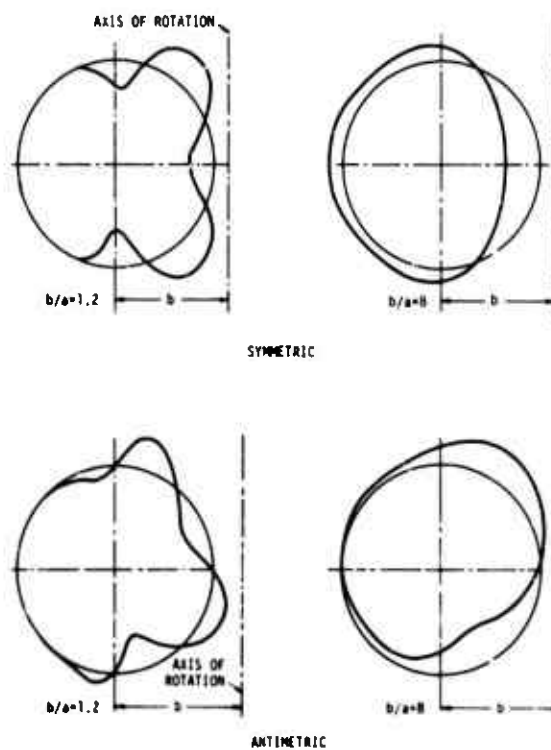
Figure 2 - Some Examples of Symmetric and Antimetric Meridional
Deformation (a/h = 100, n = 2)
From Reference 3.

3

MODEL DESIGN

In order to ensure that the models would buckle elastically, it was necessary that the buckling stresses be below the proportional limit of the material. This required that the model material have a high ratio of proportional limit to Young's modulus and was the prime consideration in the selection of the material for the models. Other factors influencing the material selection were cost and ease of fabrication.

The material selected was a plastic formed by the mixture of equal parts by weight of Versamid 140 polyamide resin and Epon 828 resin. In addition to satisfying the previously mentioned considerations, the NSRDC shop personnel had experience in the techniques of mixing and casting the material to obtain models free of air bubbles and cracks.

The Young's modulus of the material was determined to be 314,000 psi by the National Bureau of Standards from compression testing of one of the material specimens formed at the same time the models were cast. The test was conducted at a stress rate of 100 psi per minute and a temperature of 70-75°F which were to be the conditions for the model tests. Tuckerman optical strain gages were used to determine the strains. Young's modulus was not determined individually for each model cast. However, the NSRDC shop personnel had considerable experience in working with the plastic material and it was felt that this experience, together with careful control of the fabrication process, would insure negligible variation in the Young's modulus among the castings.

Several specimens were compression tested at NSRDC to determine the effect of varying stress rates on Young's modulus. These tests measured strain by a deflectometer which is a less accurate method than the Tuckerman gages. A variation of less than 1 percent was found in Young's modulus in the range 60-320 psi/min. Figure 3 is a typical compressive stress-strain curve for the model material obtained from the deflectometer compression tests at NSRDC. A Poisson's ratio of 0.4 was assumed for this material. This value was used in experiments by Hyman and Healey[7,8] using the same material and curing process as employed in this study.

The design of the experimental models was subject to certain constraints and requirements which will be described prior to presenting the design procedure.

The prime objective of this study is the comparison of analytical predictions and experimental results over a wide range of geometries. The model designs were based on Figure 4 which shows the relationship between the elastic buckling coefficient, based on the analysis of Sobel and Flügge, and the geometry. (This figure is from Reference 3.) Points were selected on these curves as the experimental model geometries. Because of previous experimental work by Sobel[4] for small values of a/(a+b) (0.111 and 0.1356), it was decided to emphasize higher values of this parameter in the model designs. Although Figure 4 is for $\nu = 0.3$ and the model material had a $\nu = 0.4$, good designs were obtained using this figure, and buckling pressures were calculated for $\nu = 0.4$ for comparison with experimental results.

The size of the models was influenced by the diameter of the test chamber and the minimum shell thickness obtainable. Most of the models were to be tested inside a pressure chamber whose inside diameter was 20 in. In order to provide sufficient clearance between the model and the chamber wall, the largest model dimension was limited to 19 in. NSRDC personnel experienced in casting and machining the plastic used in the models indicated the minimum thickness obtainable was 0.04 in.; hence, the minimum shell wall thickness was limited to this value in the model designs. The combination of these two constraints restricted the models to a maximum a/h ratio of 100 and also made the a/h value obtainable for a model dependent on its value of a/a+b.

The process selected for constructing the models consisted of casting half-sections of each model to the final outside model dimensions in an aluminum mold and then machining the final inside dimensions. The models were completed by gluing the halves together at their equators. Considering this procedure, it was economical to select model designs so that two or three models had the same outside dimensions, allowing them to be made from a single mold. The design procedure will now be described.

Several initial values of a/a+b were selected in the range 0.1 to 0.45 in order to obtain models at intervals over the entire range depicted in Figure 4. These initial values were approximately 0.1, 0.2, 0.3, 0.4, and 0.45. Ten models were designed, and in view of Sobel's previous experimental work at the low end of the a/a+b range, it was

5
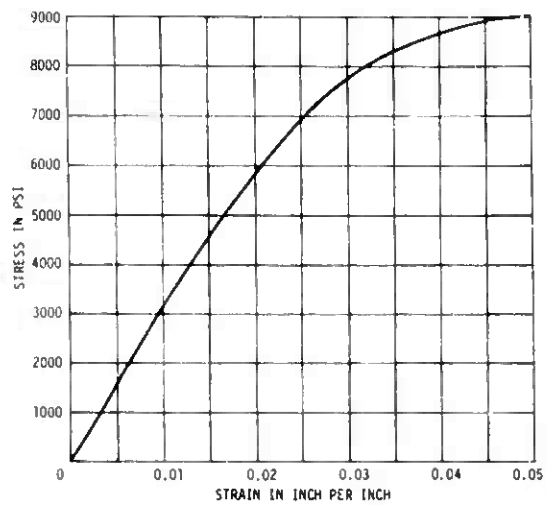
Figure 3 - Typical Compressive
Stress-Strain Curve for
Model Material
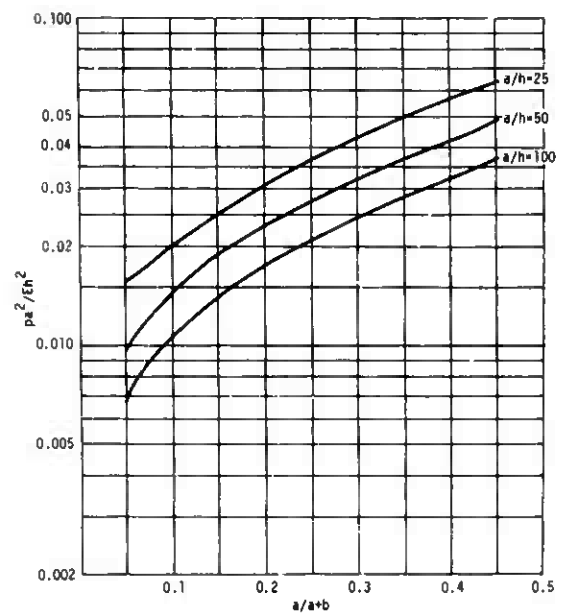
Figure 4 - Buckling Coefficients for
Toroidal Shells Under Uniform
External Pressure ($\nu = 0.3$)

From Reference 3.

TABLE 1

Toroid Model Designs

Model	a/a+b	a/h	Casting Mold
1	0.111	25	A
2	0.220	50	not cast
3	0.2183	25	B
4	0.300	50	C
5	0.298	25	C
6	0.421	100	D
7	0.420	50	D
8	0.417	25	not cast
9	0.455	100	E
10	0.453	50	E

6

decided to emphasize the middle and upper end of the range. For each value of a/a+b, various combinations of a and b were tried until values were found such that 2(a+b) was close to, but did not exceed 19 in. In order to use Figure 4, the models needed a/h values of 25, 50, or 100, as shown in the figure. Hence, for each a/a+b value, shell thicknesses were calculated for a/h values of 25, 50, and 100. It was found that certain combinations of a/a+b and a/h resulted in a shell thickness less than the minimum achievable value of 0.04 inch. For this reason, designs for a/h = 100 and a/a+b $\tilde{<}$ 0.4, and designs for a/h = 50 and a/a+b $\tilde{<}$ 0.2 could not be built with the technique selected for model construction. At this point, the designs were almost in their final form.

It was decided to alter the designs slightly so that more than one model could be cast in a single mold, since models with similar a/a+b ratios had almost the same overall diameter (2(a+b)+h) which would be the mold diameter. This was accomplished by altering the shell thickness and the dimension a to achieve the same value for (2(a+b)+h) for all models with similar a/a+b values. The dimension b and the a/h value were kept constant. The values used for (2(a+b)+h) and b were those of the highest a/h design within the group having similar a/a+b values. As a result of these dimensional alterations, models with different a/h values originally having the same a/a+b values now had a/a+b values differing slightly from each other, and the designs were dimensioned so that the ten models could be cast in five molds. Table 1 shows the design values of a/a+b and a/h and indicates which models were cast in the same mold. Models 2 and 8 were not built because of time and cost limitations.

In order to ensure that the models would fail by elastic buckling, the stresses at the buckling pressure were calculated using the following equations from page 33 of Reference 9 which are based on the linear membrane theory of toroidal shells.

$$\sigma_\theta = \frac{p}{2}\left(\frac{a}{h}\right)$$

$$\sigma_\phi = \frac{p\left(\frac{a}{h}\right)}{a\sin\phi + b}\left(\frac{a}{2}\sin\phi + b\right)$$

7

Elastic buckling pressures were obtained from Figure 4 for each design. A
design value of 325,000 psi was used for Young's modulus. Calculations
showed that all stresses calculated were well below the yield strength of
the material, and no stresses were higher than 1600 psi. Since Figure 4
is for $\nu = 0.3$, and the models have $\nu = 0.4$, the stresses were recalculated
when buckling pressures for $\nu = 0.4$ were computed. Again it was found that
the stresses were well within the elastic range of the material, and no
stresses exceeded 1900 psi.

It is known that the use of linear membrane theory results in dis-
continuous displacements in the crown region ($\phi = 0$ deg and 180 deg) of
the toroid.[10-12] These discontinuities are eliminated in thin shell toroids
by using a nonlinear membrane theory[10,12] in which the determination of
the forces is based on the deformed shape rather than, as in the linear
theory, on the undeformed shape. Also, while the strains are assumed to
be small, their derivatives are allowed to become large in the nonlinear
membrane theory. Comparisons have been made between stresses calculated
by linear and nonlinear membrane theories for thin toroids[10-12] with the
result that the differences are of minor importance for design purposes.
This is because the largest difference (on the order of 20 percent)[10]
occurs in the circumferential stress; however, the circumferential stress
is always lower than the meridional stress in a toroid, and the meridional
stresses are almost identical to each other for the two theories.

MODEL FABRICATION

It was decided to build the toroid models by casting half sections
to the final outside dimensions in female molds and machining the final
inside dimensions. A machined joint was used in both halves of the model
to aid in joining the halves together. Other fabrication techniques for
constructing shells of revolution were available, including explosive
forming metal shell halves and welding the halves together,[13] electroform-
ing the complete shell using a wax mandril,[14] vacuum forming plastic on a
male mold,[15] and pouring molten plastic over a male mold and curing to a
hard shell.[7,8]

8

Several factors entered into the decision of which fabrication technique to use. The use of plastic eliminated explosive forming from consideration. Vacuum forming would have required the use of a different type of plastic and would have been a more costly process. Pouring molten plastic over a male mold would have been satisfactory for the thinner shell designs, but to make the thicker toroids, it would have been necessary to build up layers of the plastic which could have resulted in nonuniform material properties. The chosen technique was thought to be a reliable one which would produce models of uniformly high quality and constant material properties.

Figure 5 shows the apparatus used in casting the toroidal half sections. The casting surfaces of the aluminum molds were machined to a 32 finish so that the outer surface of the casting would be smooth and not require further machining. The cavity radius and other critical mold dimensions were held to a tolerance of +0.001 in. The wood cores were used to avoid casting a large cross section and to reduce the amount of machining required. A large cross section could have caused cracking in the casting while curing for the following reason: The chemical reaction of the plastic during curing is one that develops heat. In a large cross section, the surface near the aluminum mold would be cooler than the interior of the casting, and this uneven temperature distribution could cause cracking in the hardened casting. The use of wood cores avoided this problem by keeping the casting cross section to a minimum (approximately 1/4 in. thick).

The fabrication sequence for a typical toroidal shell began with heating the aluminum mold to 110°F in an oven. The Versamid 140 and Shell Epon 828, not yet mixed, were heated to 125°F. The wood core was wrapped with cellophane tape to provide a nonporous smooth surface and then coated with a silicone grease as a parting agent (Figure 6a). This core preparation was the result of much trial and error directed at solving the problem of the core being difficult and at times impossible to remove from the cured casting. This was due to the wood grain providing a hold for the casting to resist the removal of the core. Another more expensive solution to the problem would have been to machine an aluminum core. The mold was removed from the oven and brushed with polyvinal alcohol as a
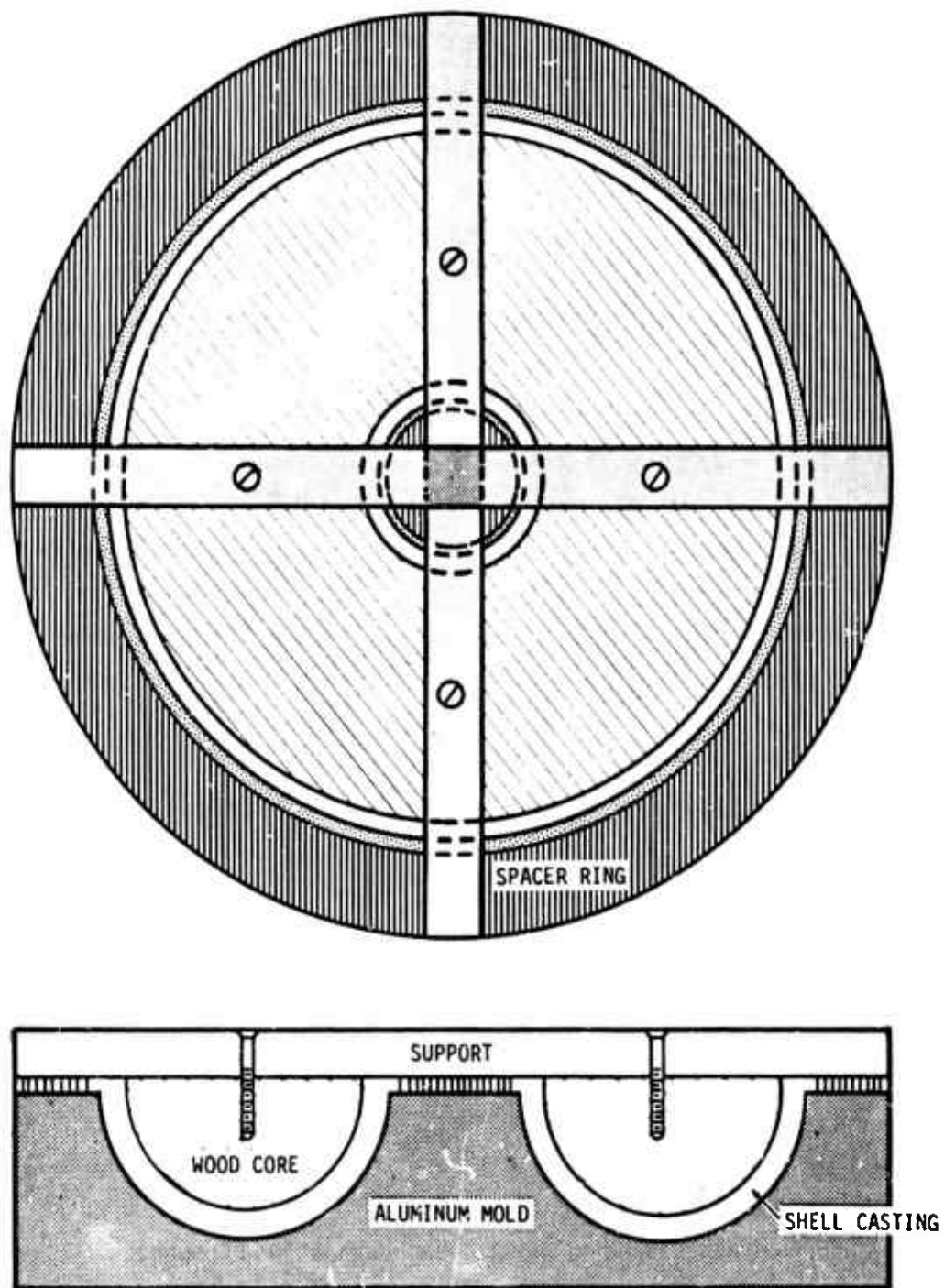
9

Figure 5 - Typical Casting Fixture for Toroid Models

10

parting agent (Figure 6b). The core was then placed in the mold and supported by spacer rings (Figure 6c). The rings and top edge of the core were beveled to allow easy removal after the casting hardened. Clamps were used to prevent movement of the core after it was centered in the mold. Figure 5 shows the complete setup in detail.

The Versamid 140 and Shell Epon 828 were removed from the 125°F oven, carefully weighed and mixed to make a mixture of equal weights of Versamid and Shell Epon. This mixture was poured into the mold from the outer edge, and flowed around the core and up to the inner edge, pushing the air ahead of it (Figure 6d). The mixture was poured until it was just below the top edge of the inner and outer spacer rings. The casting was cured by allowing the mold to remain undisturbed for 24 hours at room temperature (70-80°F). After the casting had cured, the core and spacer rings were removed from the mold. The casting was not removed from the mold at this time, but was inspected for any flaws or air pockets.

The mold and casting were then mounted on a lathe for machining of the inner surface to the final radius and forming the joint on the inner and outer edges (Figure 6e). After the machining, the finished half shell was removed from the mold. It was found that gently pulling the shell away from the mold at the outer edge and directing an air stream into the space helped to free the shell from the mold. Figure 6f shows the two halves of a typical toroidal model ready to be joined. The machined joint on the inner and outer edges can be seen in this figure. The completed halves were stored in a constant temperature room until assembly to prevent deformation due to day-night temperature fluctuations. The constant temperature room was maintained at 70-75°F and 40 percent humidity.

Prior to joining the halves of each model, thickness measurements were taken using an Ames dial gage. Table 2 presents the measured thickness for each model and a comparison with the design thickness desired. It is seen that the average measured thicknesses differ from the design values by 7.5 percent or less. The measured variation indicates the degree of nonuniformity in the measured thickness of each model and is the difference between the maximum measured thickness and the minimum measured thickness expressed as a percentage of the minimum measurement. For several models this variation is greater than 10 percent.

11

Figure 6 - Steps in Model Construction
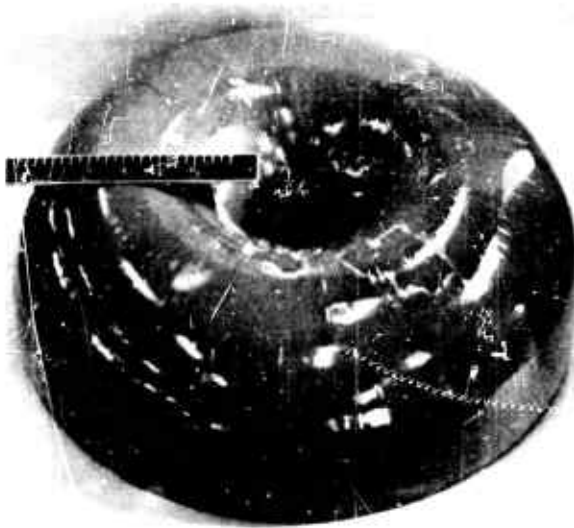
Figure 6a - Wood Core Prepared
for Casting

Figure 6b - Applying Parting Agent
to Mold
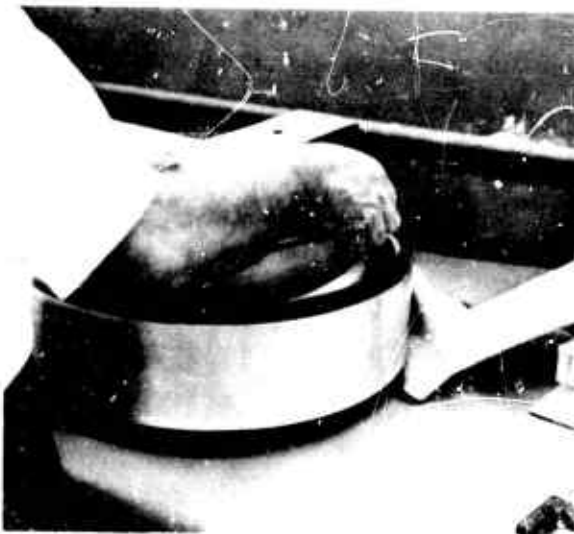
Figure 6c - Placing Wood Core
in Mold
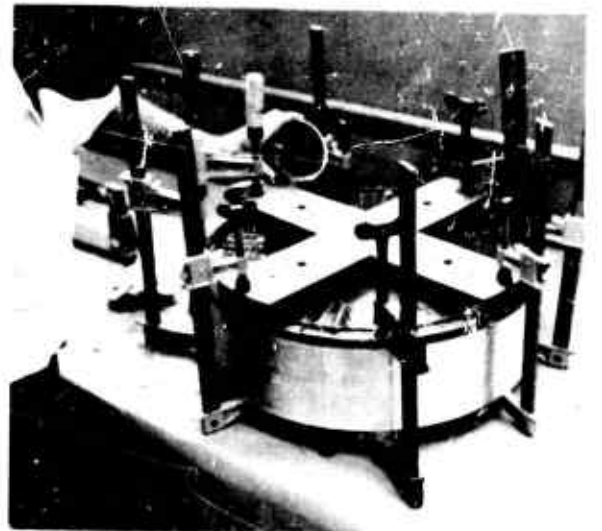
Figure 6d - Pouring Liquid Plastic
into Mold
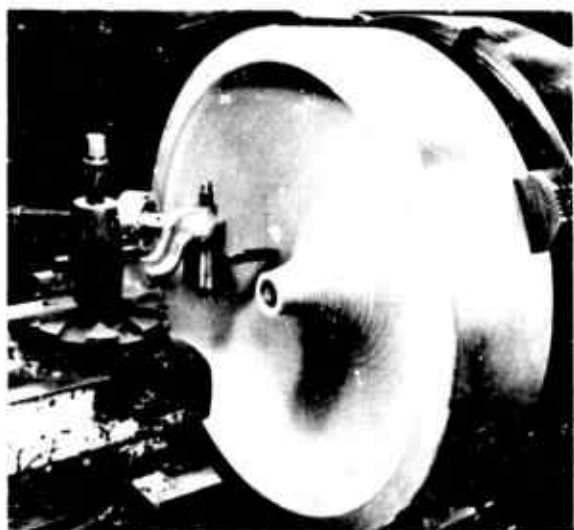
Figure 6e - Machining Inner Surface
of Shell
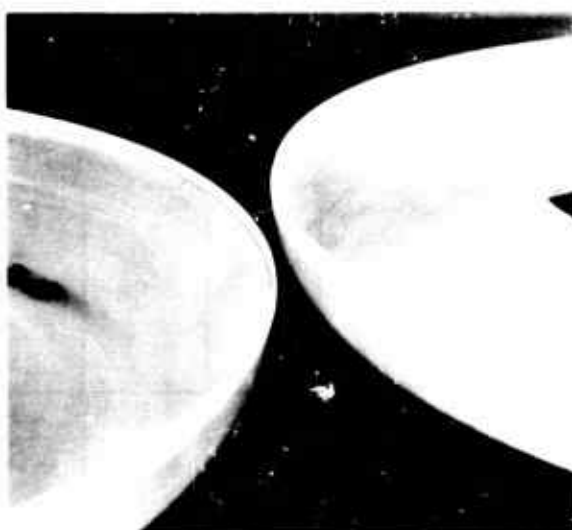
Figure 6f - Shell Halves Prior
to Joining
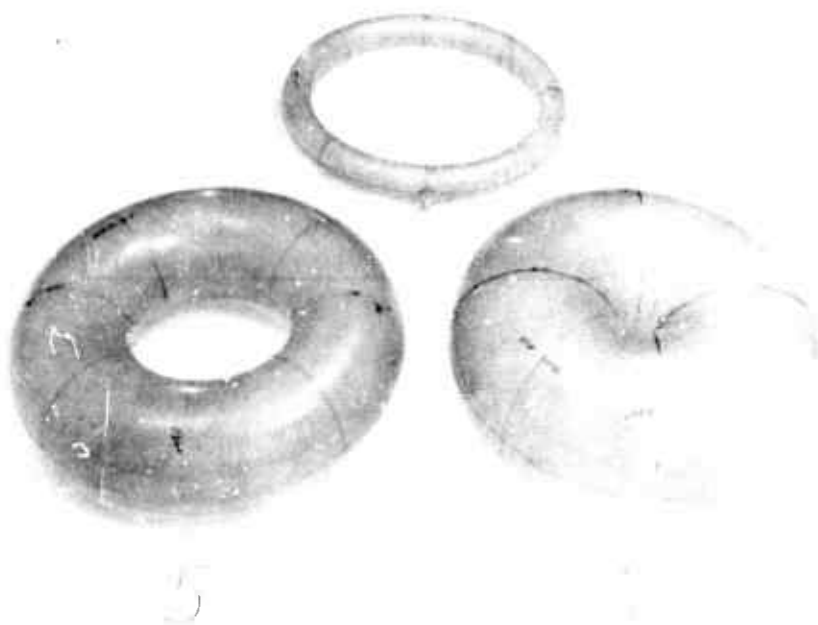
Figure 6g - Three Completed Toroid Models
(Models 1, 5, 10)

TABLE 2

Shell Thicknesses

Model	T_0 in.	T_A in.	$\dfrac{T_A}{T_D}$	Measured Variation $\dfrac{T_{max} - T_{min}}{T_{min}}$ percent
1	0.040	0.043	1.075	7.3
3	0.079	0.080	1.013	25.0
4	0.055	0.0575	1.045	5.4
5	0.109	0.116	1.064	15.0
6	0.040	0.043	1.075	20.0
7	0.080	0.082	1.025	6.3
9	0.040	0.038	0.950	14.0
10	0.080	0.084	1.050	6.3

Notes
Subscript 0 indicates design value.

Subscript A indicates average measured value.

14

The model halves were joined together using the same mixture of Versamid and Shell Epon as was used in casting the shells. Figure 6g shows three models representative of the range of geometries included in this study. A 1/16-in. diameter hole was made at the outer equator of each model, and a hollow plastic vent tube was attached to the shell over the hole. On Models 1, 3, 5, 7, and 10 this tube was attached with an epoxy cement using a small plastic collar for support. After the test of Model 1, many cracks were visible in the shell near the attachment, indicating that the cementing of the collar and tube to the shell with the brittle epoxy restricted the shell deformation in this area. The thinner the shell and the greater the curvature, the more significant would be this effect. Cracks in this area were not observed on previous tests of Models 3, 5, 7, and 10. On subsequent Models 4, 6, and 9, the vent tube was attached with Coast Pro-Seal 890 which is a flexible cement. This provided a good attachment and offered no restriction to shell deformation. The hollow plastic vent tube served a dual role: it was the means of supporting the model free and clear during the test, and it was an air passageway from the interior of the model. As a check on the circularity of the complete toroid model, measurements were taken of the outer-edge diameter (D) and the meridional cross section diameter (d) and are presented in Table 3. The measured variation gives the deviation from a perfect circle based on maximum and minimum measured dimensions. These measurements indicate negligible variation in D and a small, but perhaps significant variation in d. Table 4 compares the design values of geometric parameters a and b with the values based on average measured diameters and thicknesses. It is seen that agreement is very good.

TESTING

Two testing schemes were used in the experimental program. Models 1, 3, 5, 7, and 10 were tested using the apparatus diagrammed in Figure 7. In this scheme, the load was applied by pressurizing a tank containing the model. The interior of the model was vented to the atmosphere through a hollow plastic tube from which the model was supported in the tank. This scheme did not permit visual observation of the model during testing. A second scheme was used for Models 4, 6, and 9 which did allow the model to

15

TABLE 3

Circularity Measurements

Model	O_D in.	O_A in.	Measured Variation $\dfrac{O_{max}-O_{min}}{O_{min}}$ percent	d_O in.	d_A in.	Measured Variation $\dfrac{d_{max}-d_{min}}{d_{min}}$ percent
1	18.040	18.078	0.04	2.040	2.049	0.9
3	18.224	18.182	0.09	4.040	4.038	0.9
4	18.387	18.353	0.03	5.555	5.541	3.1
5	18.387	18.303	0.09	5.555	5.552	1.4
6	19.040	18.963	0.07	8.040	8.020	2.4
7	19.040	18.995	0.2	8.040	8.100	1.7
9	17.640	17.606	0.1	8.040	8.050	0.9
10	17.640	17.547	0.06	8.040	8.070	1.2

Subscript O indicates design value.
Subscript A indicates average measured value.
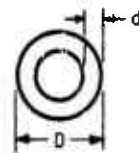
TABLE 4

Geometric Model Parameters a and b

Model	a_O in.	a_A in.	$\dfrac{a_A}{a_O}$ in.	b_O in.	b_A in.	$\dfrac{b_A}{b_O}$ in.
1	1.000	1.003	1.003	8.000	7.965	0.996
3	1.981	1.979	0.999	7.092	7.072	0.997
4	2.750	2.742	0.997	6.416	6.406	0.998
5	2.723	2.719	0.999	6.416	6.376	0.994
6	4.000	3.988	0.997	5.500	5.472	0.995
7	3.980	4.009	1.007	5.500	5.448	0.991
9	4.000	4.006	1.002	4.000	4.778	0.995
10	3.980	3.993	1.003	4.800	4.739	0.987

Subscript O indicates design value.
Subscript A indicates value calculated from average measured diameter and thickness.
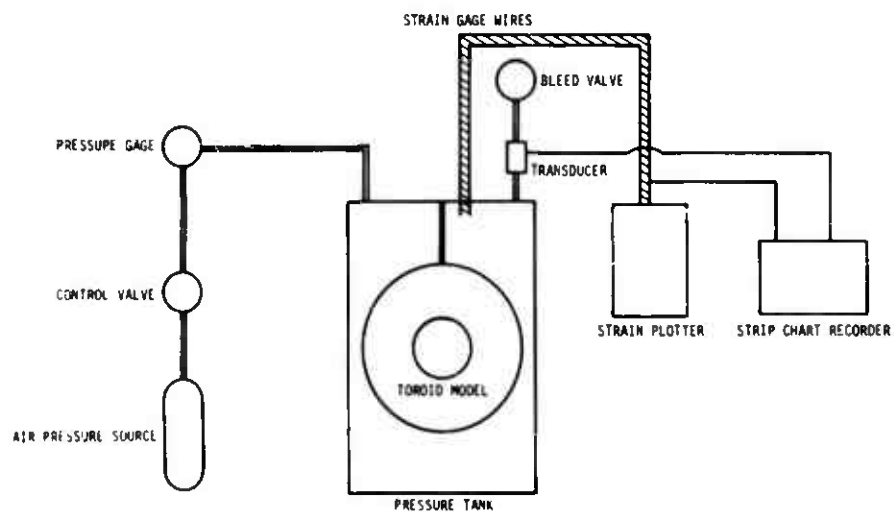
Figure 7 - Schematic Diagram of Test Apparatus for Models 1, 3, 5, 7, 10

16

be observed and photographed during testing. The apparatus for this test method is diagrammed in Figure 8. This was a vacuum type test in which the air inside the model was partially removed so that atmospheric pressure provided the load.

Electrical resistance strain gages were applied to the outer surface of most of the models to compare experimental strains with calculated membrane strains, to determine the buckling mode, and to see if the buckling strains were elastic. The degree to which each model was strain gaged was influenced by the testing scheme used and the results of preceding tests in the experimental program. The gages were applied so as to measure strain in the circumferential and meridional directions. Models 1, 3, 5, and 10 were the most extensively gaged models, Model 7 was not gaged for reasons which will be discussed later, and Models 4, 6, and 9 were observed visually and photographed and carried only one gage. The gages were Bud Metalfilm C40-111D-R2VC two-element rosette gages, temperature-compensated for plastic, with elements oriented perpendicular to each other.

It was recognized that gage heating due to the applied gage voltage during the test could cause the plastic to soften and produce a drift in the gage reading. To investigate this possibility, a gage was applied to a piece of the model material having the thickness of the thinnest toroidal shell. Gage voltages from 0.5 to 2.5 volts were applied in increments, each increment being held for 45 min. It was found that a voltage of 1 volt or less produced negligible drift; hence, during the model tests, a gage voltage of 1 volt was used. Lower voltages would have decreased the sensitivity of the recording instruments.

Models 10, 7, 3, 5, and 1 were tested in that order using the scheme depicted in Figure 7. The locations of the strain gages on these models are shown in Figures 9, 10, 11, and 12. The number of gages used per model increased with each succeeding model test in order to more fully determine the model behavior. The gage pattern used on Model 1 provided a very good determination of the model behavior. Model 7 was not gaged for the following reason: After Model 10 was tested, it was apparent that the desired stress rate of 90 psi/min. could not be achieved due to the time required to read the gages at each pressure increment. It was then decided
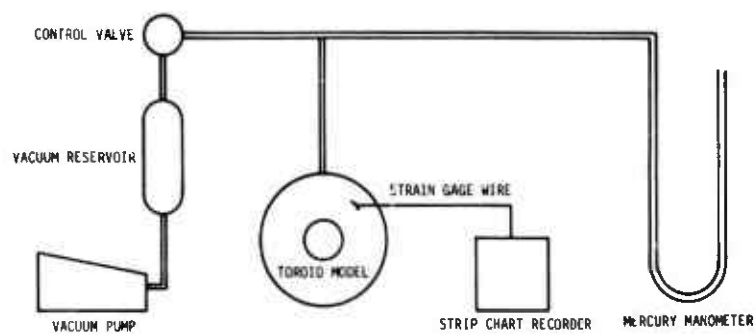
17

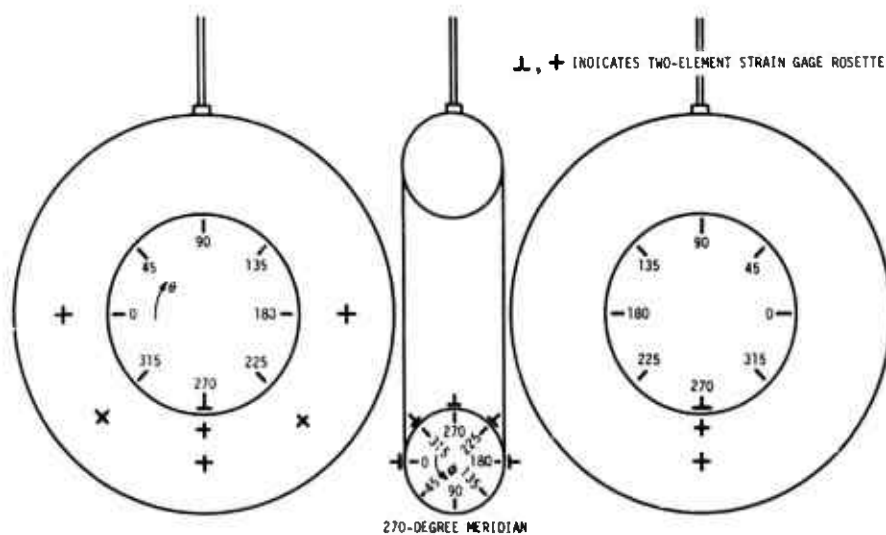Figure 8 - Schematic Diagram of Test Apparatus for Models 4, 6, 9

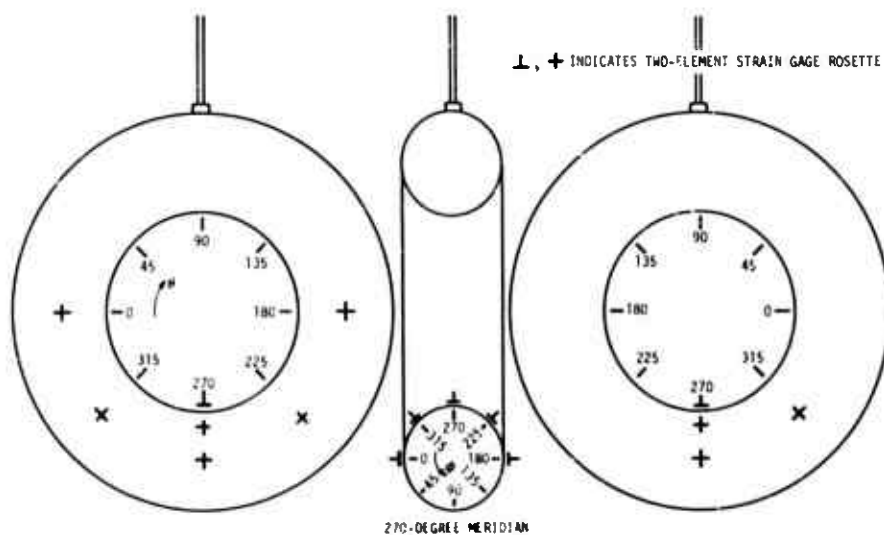Figure 9 - Strain Gage Locations for Model 10
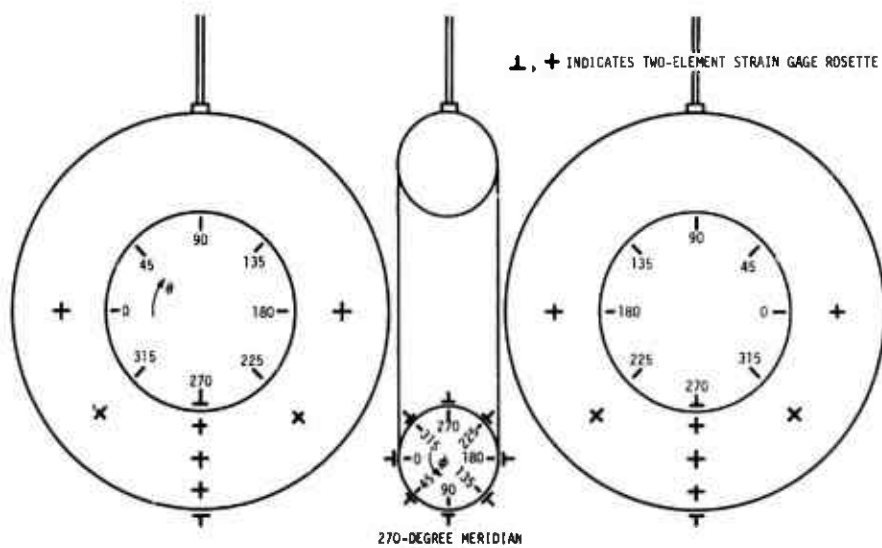

Figure 10 - Strain Gage Locations for Model 3

18

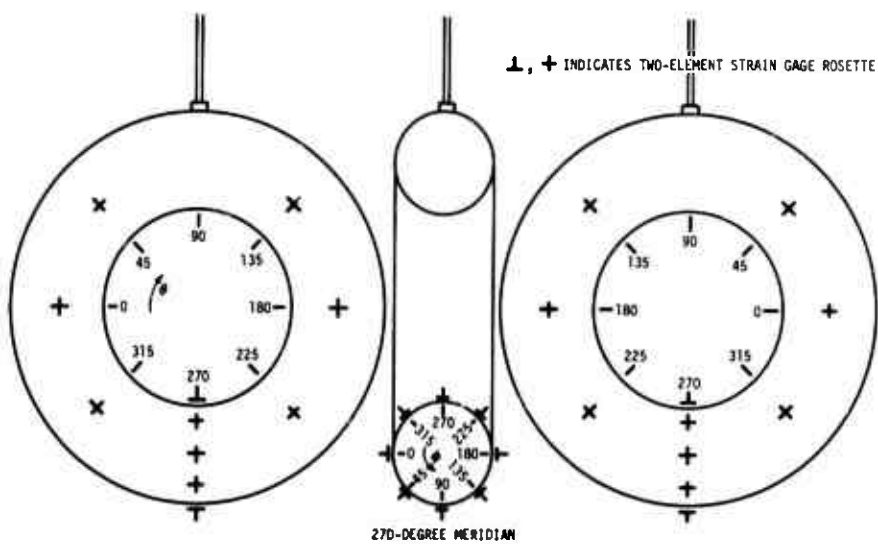Figure 11 - Strain Gage Locations for Model 5

Figure 12 - Strain Gage Locations for Model 1

19

to omit gages from Model 7 and test at the 90 psi/min. stress rate to detect any effect of the altered stress rate on the model behavior. The 90 psi/min. rate was chosen because it had been used by Hyman and Healey[7,8] in experiments on models of the same material as used in this study.

The test apparatus shown in Figure 7 will now be described. The model was suspended in the pressure tank from the vent tube and did not touch the tank walls or bottom. The tube was attached to a pressure fitting which passed through the top of the tank. The vent tube was open to the atmosphere, subjecting the interior of the model to atmospheric pressure during the test. The pressure fitting was also used to pass the strain gage wires out of the pressure tank to the recording equipment which consisted of a 48-channel strain plotter and a 2-channel strip chart recorder. At each pressure increment during the test, the strain plotter recorded the strain measured by each gage element. This resulted in a point plot of strain versus pressure for each gage element. The strip chart recorder continuously monitored one strain gage element and the pressure applied to the model. One channel was connected to a strain gage element and provided a continuous plot of strain versus time. This plot detected any creep taking place at that gage location. The second channel recorded the pressure on the model versus time. A pressure transducer connected to an opening in the tank top provided the pressure reading. All of the recording instruments were carefully calibrated before each test. The pressure in the tank was regulated by the control valve, and the bleed valve was used to relieve the tank pressure at the end of a test phase.

Models 1, 5, and 10 were each subjected to three pressure runs, the third ending in failure of the model. The first run loaded the model to half its theoretical buckling pressure. The second run applied load until nonlinearity was observed in the strain plots. The third run applied load until the model collapsed. At the end of each run the pressure on the model was completely relieved. The first run served as a checkout of the pressurizing system and the recording system. The second run detected any permanent set in the strain gages when the pressure was relieved. This would indicate yielding of the model material. Model 3 was subjected to just two pressure runs. The model failed immediately after the start of nonlinear strain behavior during the second run. Model 7 had no gages and

20

was tested in one pressure run. Each pressure run consisted of small increments of pressure after each of which strain gage readings were recorded on the strain plotter. The strip chart recorder provided a continuous record of pressure and strain. Model failure was detected by a sudden drop in pressure.

Models 9, 6, and 4 were tested last and in that order using the test apparatus diagrammed in Figure 8. The model was suspended from an overhead bracket by flexible plastic tubing connected to the vent tube at one end and to a coupling at the other end. From this coupling, plastic tubing was connected to the control valve and the manometer. The control valve, vacuum reservoir, and vacuum pump were also connected by flexible plastic tubing. A large sheet of plexiglas was placed in front of the model to protect observers from shell fragments at failure. One strain gage rosette was applied to each model at the location $\theta = 270°$, $\phi = 0°$. During the tests of Models 6 and 9, only one gage element could be recorded because of equipment limitations at the time of the test; however, both elements were recorded on Model 4. The 2-channel strip chart recorder was used to record the strains versus time. Pressure was not recorded continuously because the available transducer would not work satisfactorily with a vacuum. Pressure readings were hand marked on the strain record.

It was found that for photographic purposes, additional light would be needed on the models during the tests. This was provided by two 100-watt light bulbs placed on opposing sides of the models. In order to reduce glare, the additional light was placed on the same side of the plexiglas as the model, and the photographic angle was perpendicular to the plexiglas sheet. The camera was mounted on a tripod approximately 20 in. in front of the plexiglas, and the model was 2 in. behind it. The camera was a Polaroid black-and-white with automatic light exposure control and was manually operated during each test. The tests of Models 4 and 6 utilized mirrors to allow both crown areas ($\phi = 0°$, $\phi = 180°$) to be visible in the same photograph. These were the areas of greatest deformation.

Model 9 was tested in two pressure runs; Models 4 and 6 were each tested in three runs. Each run consisted of stepwise increases in the vacuum regulated by the control valve and indicated on the mercury

21

manometer. The low buckling pressures and the taking of photographs resulted in slower stress rates than were planned.

Table 5 gives the stress rate for each model tested. The most highly stressed location on the models, meridional stress at $\phi = 270°$, was used in determining the stress rate.

DISCUSSION OF RESULTS

Table 6 gives the comparison between the experimental collapse pressures and the analytical predictions of elastic buckling pressures for each model tested. Average measured values of geometric parameters were used in calculating the Sobel and Flügge and the Bushnell analytical predictions. Any variation between test and theory of less than 10 percent must be considered unavoidable due to the possibility of random experimental error. Hence, only variations greater than 10 percent will be considered significant in comparison with analyses. It is seen that with the exception of Models 1 and 9, the experimental collapse pressures agree with the Bushnell analytical predictions to within +10 percent. Agreement to within +10 percent is also obtained with the Sobel and Flügge analytical predictions for Models 5, 6, 7, and 10. It is noted that with the exception of Model 6, the Sobel and Flügge analysis predicts higher buckling pressures than the Bushnell analysis. This seems to indicate that the Bushnell analysis is the more conservative of the two. The fact that analyses are in significant disagreement with the experimental results for Models 1 and 9 will be discussed later. The agreement of results for Models 3 and 4 with the Bushnell analysis but not with the Sobel and Flügge analysis is of uncertain importance. It could indicate a geometric range where the Sobel and Flügge analytical predictions become too optimistic. However, more than two models are needed to make a definite determination. The factor of model stress rate does not appear to have any significant effect on model behavior for rates of 90 psi/min. or less. The experimental stress rates shown in Table 5 did not appear to influence the degree of agreement between test results and analytical predictions.

The test results will now be used to indicate the effect of imperfections on toroidal shells. Hutchinson[16] has determined that toroidal

22

TABLE 5

Experimental Stress Rates

Model	First Pressure Run psi per min	Second Pressure Run psi per min	Third Pressure Run psi per min
1	9.7	14.7	11.2
3	69.0	80.0	
4	15.1	15.1	17.2
5	44.5	37.3	28.0
6	14.0	21.0	16.0
7	88.0		
9	32.7	20.3	
10	48.0	53.0	60.0

TABLE 6

Experimental and Analytical Buckling Pressures

Model	$P_{Sobel\ and\ Flugge}$ (psi)	$P_{Bushnell}$ (psi)	$P_{Southwell}$ (psi)	$P_{experiment}$ (psi)	$\dfrac{P_{experiment}}{P_{Sobel\ and\ Flugge}}$	$\dfrac{P_{experiment}}{P_{Bushnell}}$	$\dfrac{P_{experiment}}{P_{Southwell}}$	b/a	a/h
1	12.89	11.01	8.27	8.3	0.64	0.75	1.00	8.000	25
3	17.98	15.94	15.5	15.0	0.83	0.94	0.97	3.581	25
4	4.63	4.45	4.15	4.03	0.87	0.91	0.97	2.333	50
5	25.57	23.8	23.3	23.0	0.90	0.97	0.99	2.356	25
6	1.31	1.32	1.39	1.33	1.02	1.00	0.96	1.375	100
7	6.15	5.99	--	6.4	1.04	1.07	--	1.382	50
9	1.10	1.07	1.16	1.37	1.25	1.28	1.18	1.200	100
10	7.11	7.01	6.5	7.3	1.03	1.04	.1.12	1.206	50

23

shell segments subject to uniform external pressure are for the most part imperfection-sensitive. However, no work could be found in the literature on complete toroids. The Southwell method[17] was used to calculate a collapse pressure for each model using the experimental strain data. The purpose of this method is to give the pressure at which an imperfection-free (perfect) model will fall. The validity of the Southwell calculation depends on the type of equilibrium exhibited by a perfect model at the buckling pressure. The type of equilibrium indicates the post-buckling behavior. Figure 13 depicts the neutral, stable, and unstable equilibrium states. The solid lines indicate the post-buckling behavior of perfect models. The dashed lines indicate the behavior of imperfect models. Since no model can be constructed completely free of imperfections, all experimental models fall into the imperfect model category. As shown in Figure 13a, for a neutral equilibrium state, the load on an imperfect model asymptotically approaches the buckling pressure from below as deflections increase. Collapse occurs at or slightly below the theoretical pressure. Near the buckling pressure, deflections can increase with no increase in load. If the model can sustain large deflections, and the perfect shell is of a stable equilibrium state, Figure 13b, then the pressure can be increased above the theoretical buckling pressure before the model collapses. If a perfect shell is of the neutral or stable equilibrium state, then the imperfect model is said to be insensitive to imperfections because imperfections do not cause a significant reduction in the collapse pressure compared to the theoretical buckling pressure for a perfect shell. An imperfect model is sensitive to imperfections if the perfect shell is of an unstable equilibrium state as shown in Figure 13c. The effect of imperfections is to cause the model to fail at a pressure significantly less than the theoretical buckling pressure. This type of behavior is characterized by the complete spherical shell.

The Southwell method is valid only for the neutral equilibrium state. According to Roorda,[18] the Southwell method overestimates the buckling pressure for a stable equilibrium state and underestimates it for an unstable state. The fact that most of the model results in Table 6 are in good agreement with one or both analyses indicates a neutral equilibrium state and, hence, insensitivity to imperfections. The close agreement
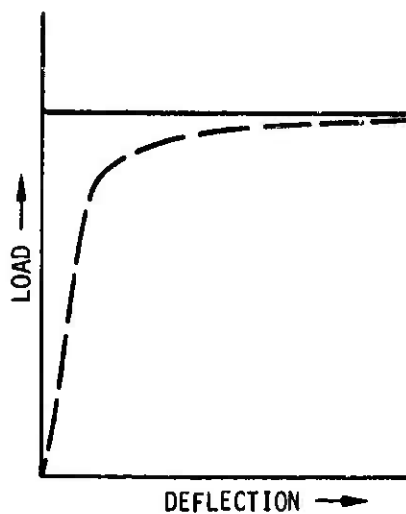
24

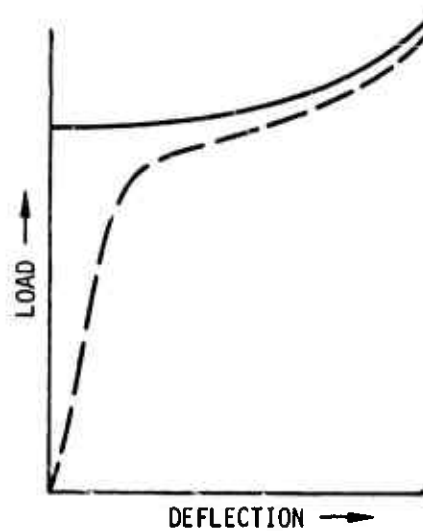Figure 13a - Neutral Equilibrium   Figure 13b - Stable Equilibrium
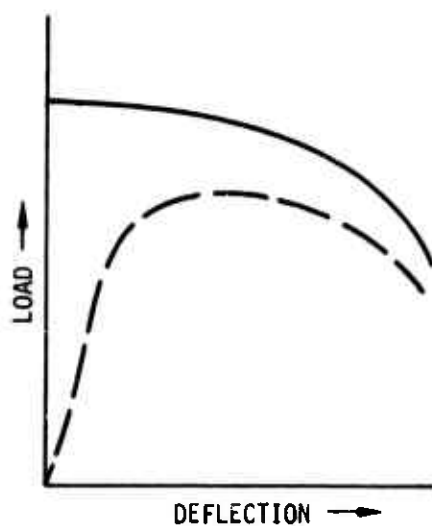

Figure 13c - Unstable Equilibrium

Figure 13 - Equilibrium States

between test pressures and Southwell pressures for Models 1, 3, 4, 5, and 6 also indicates insensitivity to imperfections. Imperfection sensitivity would be indicated if the Southwell pressures were significantly above the test pressures. None of the Southwell pressures calculated were significantly above the test pressures.

The results of the test of Model 1 can be interpreted in several ways. On examination of the model after failure, it was observed that the area of failure was a 90-deg segment in the circumferential direction which included the point of attachment of the vent tube. Much local cracking was evident in the shell near the vent tube. The remainder of the model was intact. The model could have undergone a premature failure caused by a too rigid attachment of the vent tube to the shell. This could have created a local hard spot, preventing the shell from deforming at this location during the test. This, in combination with the high meridional curvature, might have caused cracking at low pressures. However, it is surprising to see the agreement of the Southwell pressure with the test result. This seems to indicate that the model collapsed at the buckling pressure of a perfect model, indicating overly optimistic analytical predictions. Sobel[3,4] has tested models with the same b/a ratio as Model 1, but with higher a/h values (70-80) and obtained good agreement ($\pm$10 percent) with analytical predictions. Possibly for b/a = 8 and a/h = 25, the analysis gives results which are too high. Another interpretation of the results is that the geometry has unstable equilibrium and the Southwell calculation underestimates the buckling pressure. The model would then be sensitive to imperfections and fail at a pressure significantly less than the analytical prediction, and the Southwell pressure would be too low. In this interpretation, the analytical predictions would be correct. Another test of the same model geometry without a hard spot is needed to resolve the question.

The experimental collapse pressure of Model 9 is significantly greater than the analytical predictions and the Southwell pressure. This is a strong indication that the model failed in the post-buckling region, was of the stable equilibrium type, and was not imperfection-sensitive. Since the Southwell method overestimates for stable equilibrium, the perfect model buckling pressure is actually closer to the analytical

26

predictions than the calculated Southwell pressure. This interpretation
of the test results for Model 9 is in agreement with the behavior observed
and photographed as shown in Figure 14. The first visible deflection
occurred at a pressure of 65 percent of collapse load. Succeeding incre-
ments of load produced greater deflections until failure occurred.

Models 4 and 6 were also visually observed and photographed.
Figure 15 shows deflections of Model 6. The first visible deflection
occurred at 85 percent of collapse load. However, in view of the good
agreement of experimental collapse pressure with analytical predictions
and with the Southwell pressure, these deflections must be interpreted as
large prebuckling deformations caused by imperfections. It appears that
the neutral equilibrium state applies to Model 6 and, hence, the model was
insensitive to imperfections. The deflections of Model 4 are shown in
Figure 16. The first visible deflections occurred at the collapse pressure
and increased with no increase in pressure. Considering this and the
close agreement of the test result with one of the analytical predictions
and with the Southwell pressure, a neutral equilibrium state for the
perfect shell is indicated. As with Model 6, this indicates insensitivity
to imperfections.

The results of Model 10 are subject to two interpretations. The
experimental collapse pressure is in good agreement with the analytical
predictions but is significantly greater than the Southwell pressure.
While the agreement of test and analysis indicates neutral equilibrium,
the lower Southwell pressure points to stable equilibrium. In either
event, insensitivity to imperfections is indicated.

Table 7 compares the analytical buckling mode prediction and the
experimental mode determination using measured strains and photographs.
With the exception of Model 1, both analyses predict the same mode for
each model. The circumferential wave number (n) for each model was
determined either by studying the photographs taken during the test or by
plotting the total circumferential strain near the collapse pressure of
each of the crown gages and noting the resulting pattern. By comparing
meridional strains on either side of the 90-270° meridional diameter, a
determination of symmetric or antimetric deformation was made. Using the
photographs, this was done by noting the deformations of opposing crown

27

Figure 14a - No Load

Figure 14b - 0.89 PSI, 65 Percent
Collapse Load, First Visible De-
formation

Figure 14c - 1.08 PSI, 79 Percent
Collapse Load

Figure 14d - 1.22 PSI, 89 Percent
Collapse Load

Figure 14e - 1.37 PSI, 100 Percent
Collapse Load, Just Before Col-
lapse

Figure 14f - After Failure

Figure 14 - Deformation of Model 9 During Test

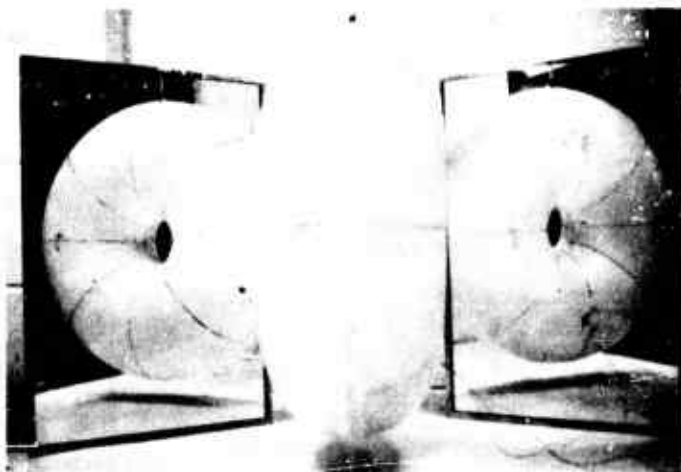Figure 15 - Deformation of Model 6 During Test

Figure 15a - No Load

Figure 15b - 1.13 PSI, 85 Percent Collapse
Load, First Visible Deformation

Figure 15c - 1.28 PSI, 96 Percent
Collapse Load

29

Figure 15d - 1.33 PSI, 100 Percent
Collapse Load, Just Before Col-
lapse

Figure 15e - After Failure

Figure 16 - Deformation of Model 4 During Test

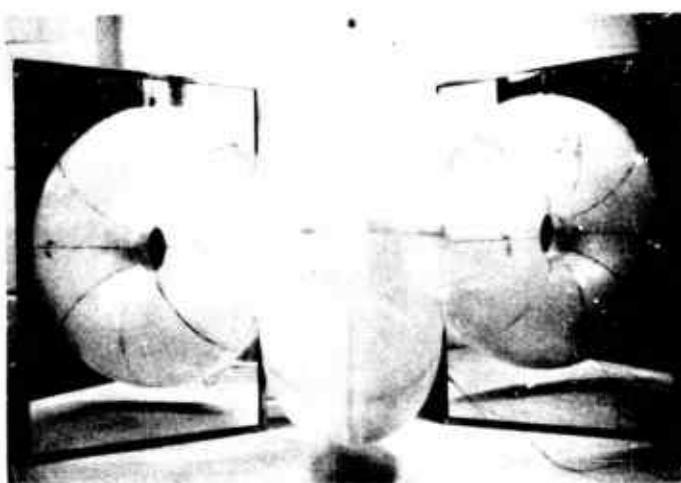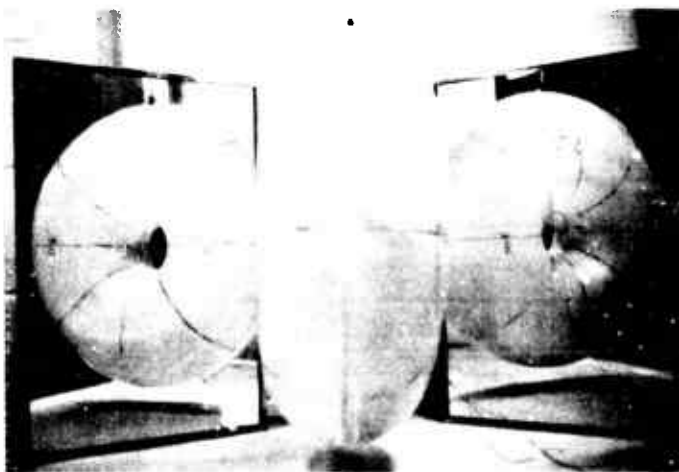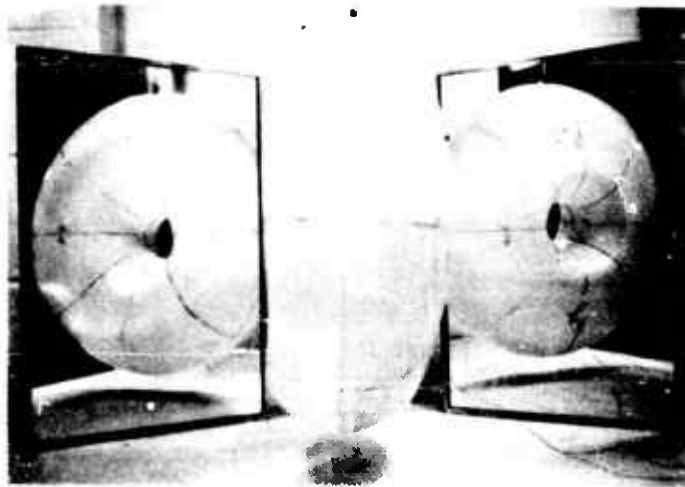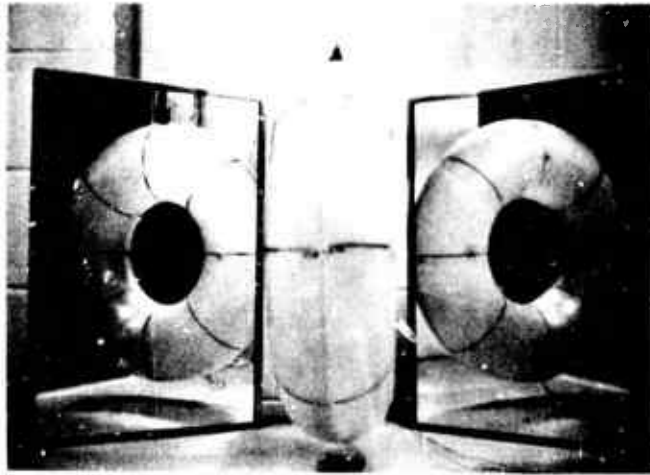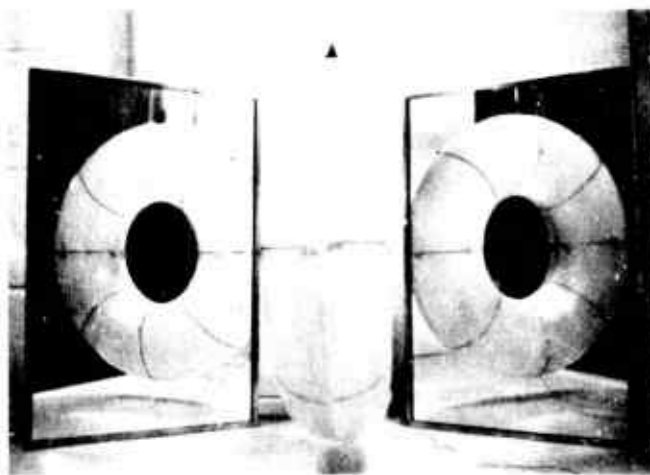

Figure 16a - No Load

Figure 16b - 4.03 PSI, 100 Percent Collapse
Load, First Visible Deformation
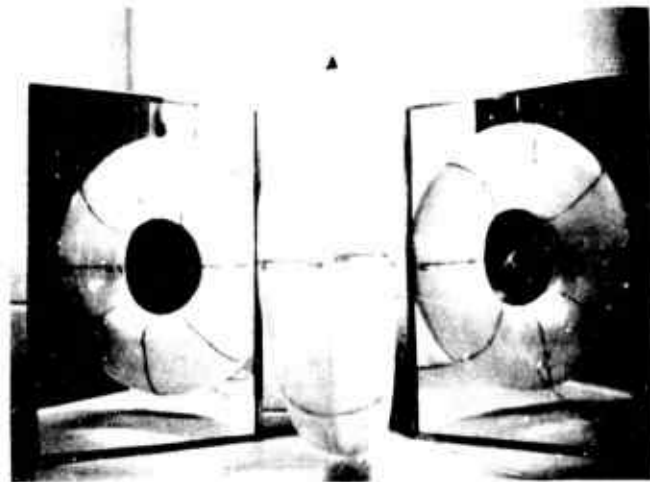
Figure 16c - 4.03 PSI, 100 Percent
Collapse Load

31
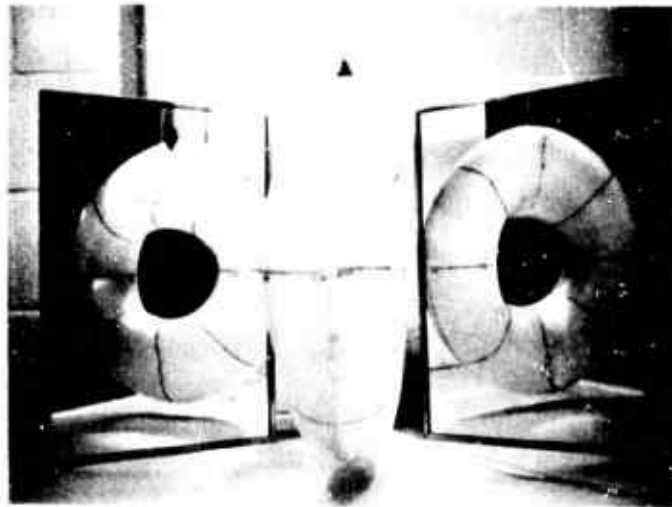
Figure 16d - 4.03 PSI, 100 Percent
Collapse Load, Just Before Failure
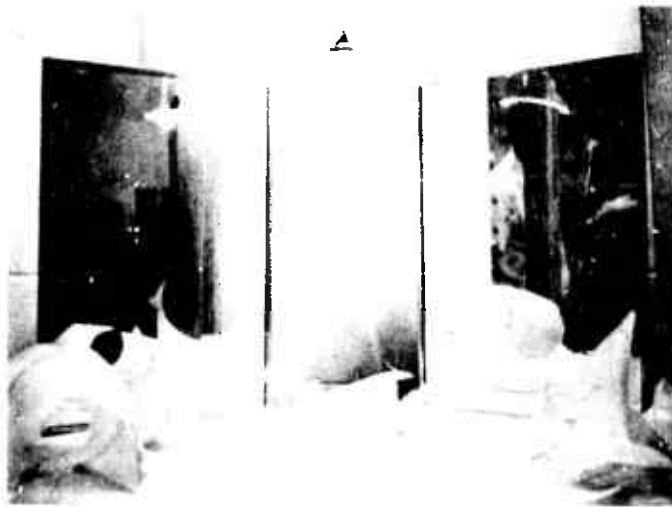
Figure 16e - After Failure

TABLE 7

Experimental and Analytical Buckling Modes

Model	Sobel and Flugge Analysis	Bushnell Analysis	Experiment	How Determined Experimentally
1	n=2 Symmetric	n=0 Antimetric	n=2 Antimetric	Strain gage
3	n=0 Antimetric	n=0 Antimetric	n=? Antimetric	Strain gage
4	n=0 Antimetric	n=0 Antimetric	n=0 or 2 Antimetric	Photograph
5	n=0 Antimetric	n=0 Antimetric	n=? Antimetric	Strain gage
6	n=0 Antimetric	n=0 Antimetric	n=0 Antimetric	Photograph
7	n=0 Antimetric	n=0 Antimetric	--	--
9	n=0 Antimetric	n=0 Antimetric	n=0 Antimetric	Photograph
10	n=0 Antimetric	n=0 Antimetric	n=? Antimetric	Strain gage

32

areas. An inward deformation on one-crown and an outward deformation on the opposite crown indicated an antimetric mode.

The experimental collapse mode of Models 4, 6, and 9 can be seen in the photographs shown in Figures 14, 15, and 16. There is some uncertainty in the wave number for Model 4. Figures 17, 18, 19, and 20 show the circumferential strain pattern for the crown areas of Models 1, 3, 5, and 10. The n=2 pattern of Model 1 is very evident. Models 3, 5, and 10 had too few gages to positively identify the buckling mode. No mode determination could be made for Model 7 since it was neither photographed nor strain gaged. In all models observed and photographed, the crown area appeared to be the area of greatest deformation.

Figures 21-27 present load-strain plots of experimental strains for each model tested. For models having many gages, the plots are for locations of maximum strain. Strains based on linear membrane theory are also shown for comparison. It is seen that the experimental strains exhibit nonlinearity in all models, which is indicative of bending. This is probably due to imperfections. For Model 1, this is also due to circumferential bending caused by the n=2 buckling mode. For most models, linear membrane strains agree significantly better with the experimental meridional strains than with the circumferential strains. This result is of particular interest in connection with the previously discussed fact that linear and nonlinear membrane theories produce almost identical meridional stresses, but differ significantly in the circumferential stresses. Even though there is disagreement between linear membrane theory and experimental strains, the good agreement between experimental buckling pressures and analytical predictions seems to justify the use of linear membrane theory in the buckling analysis.

That each model failed elastically is assured by the fact that all measured strains were elastic at collapse. The maximum strain measured at collapse was -0.013 in. per in., the meridional strain at $\theta = 270°$, $\phi = 180°$ on Model 5. Comparing this with Figure 3, it is seen that this strain is elastic. On most models, the strain at collapse was less than 0.01 in. per in. With most models, when nonlinear strains were evident during a pressure run, the load was removed to detect any permanent set in the strains. None was ever detected.

33
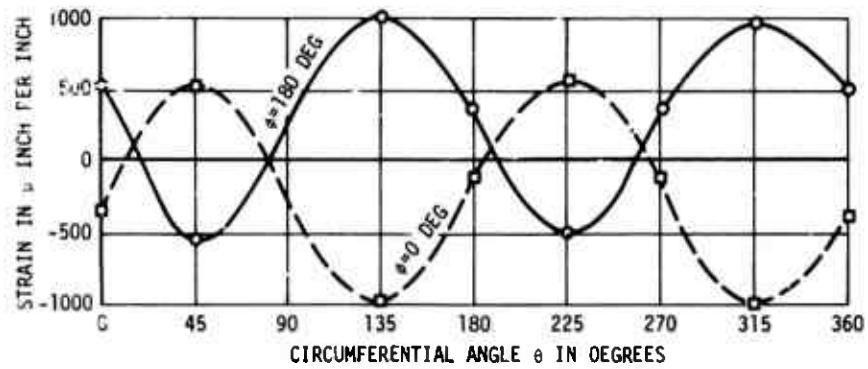
Figure 17 - Model 1, Circumferential Strains at 8 psi
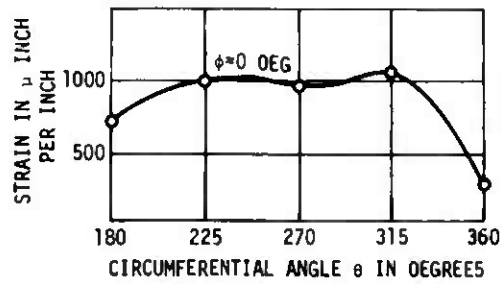
Figure 18 - Model 3, Circumferential Strains
at 14 psi
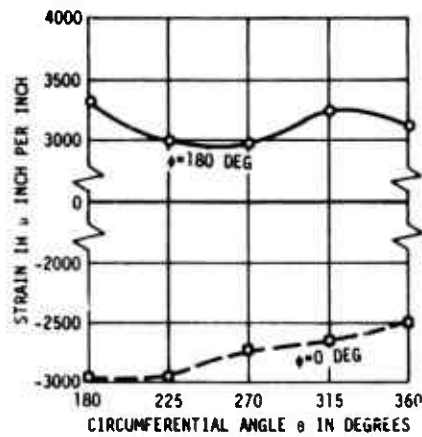
Figure 19 - Model 5, Circumferential
Strains at 22.5 psi
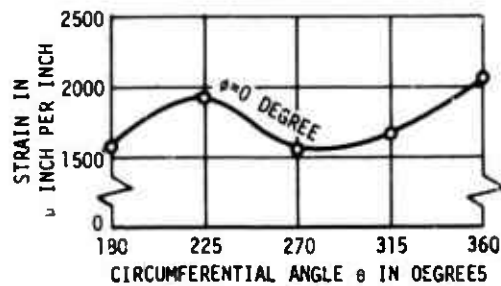
Figure 20 - Model 10, Circumferential
Strains at 5.5 psi

34
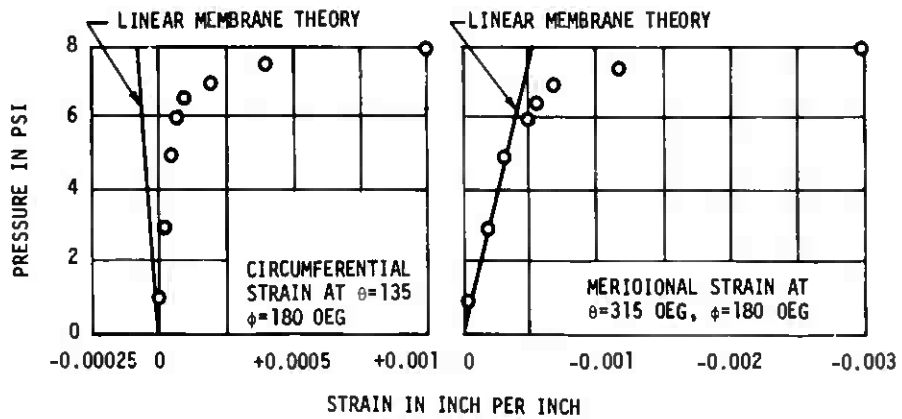
Figure 21 - Pressure versus Strain for Model 1 (Collapse
Pressure = 8.3 psi)
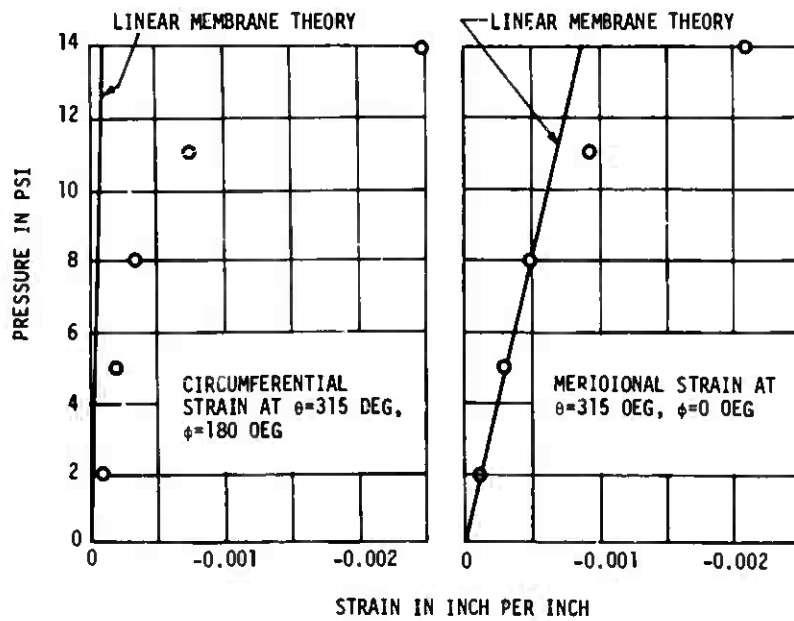
Figure 22 - Pressure versus Strain for Model 3 (Collapse
Pressure = 15 psi)

35
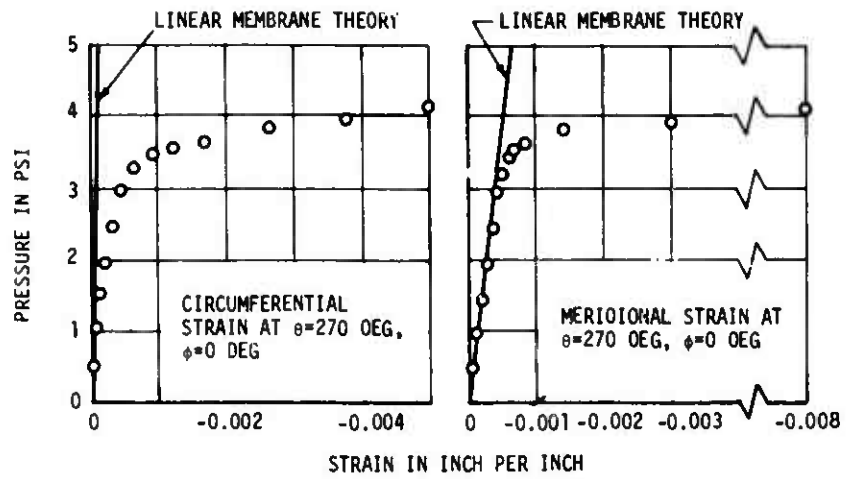
Figure 23 - Pressure versus Strain for Model 4 (Collapse
Pressure = 4.03 psi)
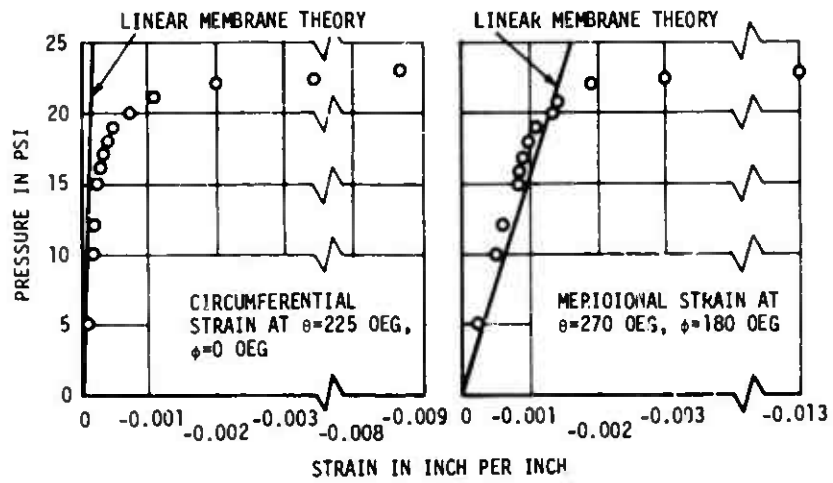
Figure 24 - Pressure versus Strain for Model 5 (Collapse
Pressure = 23 psi)
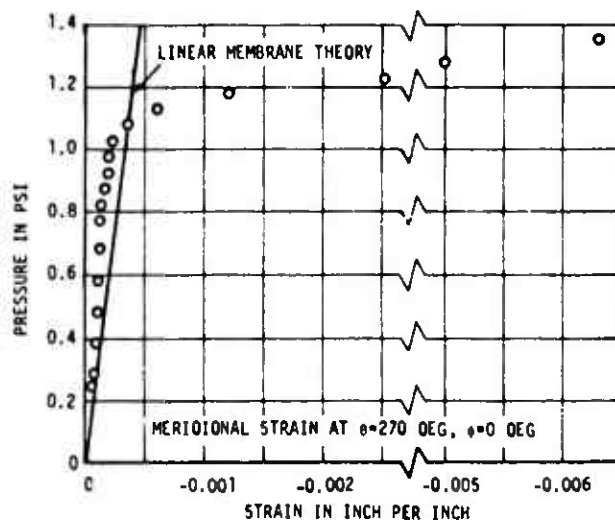
Figure 25 - Pressure versus Strain for Model 6
(Collapse Pressure = 1.33 psi)
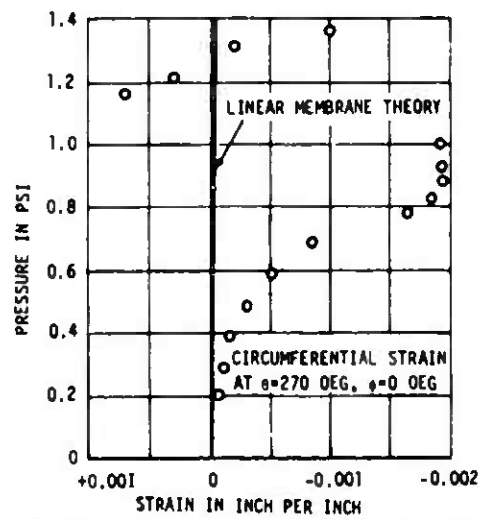
Figure 26 - Pressure versus Strain for
Model 9 (Collapse Pressure
= 1.37 psi)
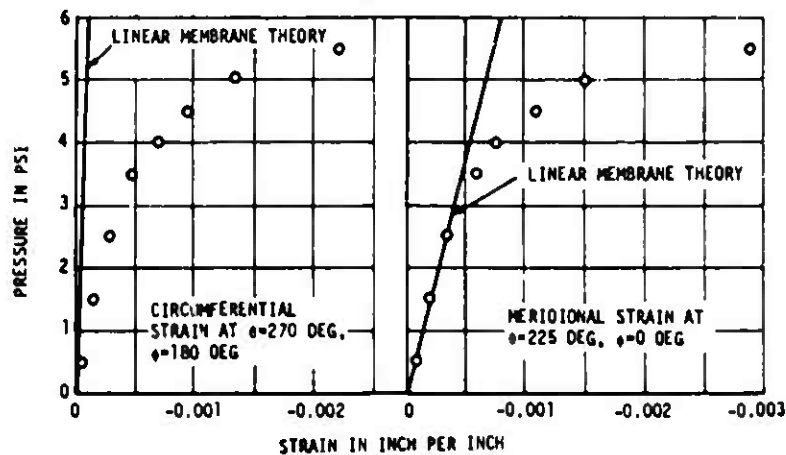
Figure 27 - Pressure versus Strain for Model 10
(Collapse Pressure = 7.3 psi)

37

Those strains which were continuously recorded along with pressure during testing increased at an accelerated rate near collapse pressures. In some cases, the strain increased with no increase in load. This would seem indicative of creep, but cannot be because strains are elastic. This is probably the result of the perfect shell having a neutral equilibrium state, causing imperfections to produce large deflections as the load-deflection curve asymptotically approaches the buckling pressure.

CONCLUSIONS

1. The Bushnell analysis agreed with test results with the exception of Model 9, which exhibited post-buckling strength, and Model 1, whose results are questionable.

2. The Sobel and Flügge analysis agreed with half the models tested. It tended to be too optimistic at b/a ratios of 2.33 and 3.58.

3. Of the two analyses, the Bushnell analysis appears to be the more conservative.

4. It was possible te experimentally determine the buckling mode of models where sufficient data was obtained from strain gages er from photographs. Strain gages are the better indicator of mode.

5. The experimental strains exhibited a high degree of nonlinearity, probably due to imperfections.

6. For most models tested, at loads up to half the collapse load, theoretical strains based on linear membrane theory were in good agreement with experimental strains for the meridional direction, but not for the circumferential direction.

7. Test results indicate that complete toroidal shells under uniform external pressure are insensitive to imperfections.

38

ACKNOWLEDGMENTS

APPENDIX

DESCRIPTION OF ANALYSES

ANALYSIS OF SOBEL AND FLÜGGE

The analysis of Sobel and Flügge for the prediction of elastic buck-
ling pressures of toroids under uniform external pressure is described in
detail in References 3 and 4. A brief description of the analysis will be
given here.

A linear membrane analysis is used for the prebuckling solution,
and buckling pressures are calculated from stability equations for a
toroid which are obtained by specialization of the stability equations of
a general shell of revolution. The stability equations for the toroid are
solved using Fourier series representations of the displacement components
developed during buckling. Buckling modes which are symmetric and anti-
metric about line A-A in Figure 1 are considered.

The following assumptions are made for this analysis.

1) The shell material is isotropic, homogeneous and obeys Hooke's
   law (linearly elastic).

2) The shell thickness is constant.

3) The shell thickness is small in comparison with the radii of
   curvature of the middle surface.

4) Normals to the middle surface before deformation remain normal
   after deformation with no change in length.

5) The normal stresses acting on surfaces parallel to the middle
   surface are small compared to other stresses and may be neglected
   in the stress-strain relations.

6) All incremental quantities are infinitesimal.

7) The incremental strains are small in comparison with the incre-
   mental rotations.

8) The basic state may be approximated by a membrane state of
   stress.

Equilibrium equations are developed for a general shell of revolu-
tion based on the deformed state of the shell. This is accomplished with
a linear stability analysis wherein the effects of prebuckling rotations
are neglected. The equations are a system of partial differential
equations with variable coefficients. For the case of axially symmetric
loading (uniform external pressure), the coefficients in the equilibrium

40

equations are independent of the circumferential coordinate (θ). Hence, separation of variables is possible which reduces the equations to ordinary differential equations. To accomplish this, the displacements, force and moment resultants, strains, and rotations in the equilibrium equations are represented with Fourier series expressions in the circumferential (θ) direction. The expressions for the displacements are (Figure 1)

$$u = \sum_{n=0}^{\infty} u_n(\phi) \cos n\theta \qquad (1a)$$

$$v = \sum_{n=1}^{\infty} v_n(\phi) \sin n\theta \qquad (1b)$$

$$w = \sum_{n=0}^{\infty} w_n(\phi) \cos n\theta \qquad (1c)$$

The equilibrium expressions are in terms of displacements, forces, moments, strains, and rotations. However, using the elastic law (relations between stress and displacement), strain-displacement relations, and curvature-displacement relations, the equilibrium equations are obtained in terms of displacements only. These equilibrium equations are the stability equations for a general shell of revolution under axially symmetric loading.

The stability equations are then specialized for the toroid geometry under uniform external pressure. The linear membrane solution from Reference 9 is used for the prebuckling stresses. The resulting stability equations for the toroid consist of three linear homogeneous ordinary differential equations with variable coefficients. The unknowns in these equations are the displacement components $u_n(\phi)$, $v_n(\phi)$, and $w_n(\phi)$. Next, the displacement components are represented by Fourier series in the meridional (φ) direction.

$$u_n(\phi) = \sum_{m=1}^{\infty} U_m \sin m\phi + \sum_{m=0}^{\infty} \tilde{U}_m \cos m\phi \qquad (2a)$$

41

$$v_n(\phi) = \sum_{m=o}^{\infty} V_m \cos m\phi + \sum_{m=1}^{\infty} \tilde{V}_m \sin m\phi \qquad (2b)$$

$$w_n(\phi) = \sum_{m=o}^{\infty} W_m \cos m\phi + \sum_{m=1}^{\infty} \tilde{W}_m \sin m\phi \qquad (2c)$$

The series with Fourier coefficients U_m, V_m, W_m represent a buckling mode which is symmetric about line A-A in Figure 1. The coefficients $\tilde{U}_m$, $\tilde{V}_m$, $\tilde{W}_m$ represent a buckling mode which is antimetric about this line.

Using equations (2) together with some trigenometric identities, the stability equations are reduced to an infinite system of linear homogeneous algebraic equations of the form

$$\sum_{m=1}^{\infty} A_m \sin m\phi + \sum_{m=o}^{\infty} \tilde{A}_m \cos m\phi = 0 \qquad (3a)$$

$$\sum_{m=o}^{\infty} B_m \cos m\phi + \sum_{m=1}^{\infty} \tilde{B}_m \sin m\phi = 0 \qquad (3b)$$

$$\sum_{m=o}^{\infty} C_m \cos m\phi + \sum_{m=1}^{\infty} \tilde{C}_m \sin m\phi = 0 \qquad (3c)$$

where

$$A_m = A_m(U_m, V_m, W_m) \quad , \quad \tilde{A}_m = \tilde{A}_m(\tilde{U}_m, \tilde{V}_m, \tilde{W}_m)$$

$$B_m = B_m(U_m, V_m, W_m) \quad , \quad \tilde{B}_m = \tilde{B}_m(\tilde{U}_m, \tilde{V}_m, \tilde{W}_m)$$

$$C_m = C_m(U_m, V_m, W_m) \quad , \quad \tilde{C}_m = \tilde{C}_m(\tilde{U}_m, \tilde{V}_m, \tilde{W}_m)$$

Since $\sin m\phi$ and $\cos m\phi$ are linearly independent, in order for equations (3) to be satisfied, we must have

42

$$A_m = B_m = C_m = 0$$

$$\tilde{A}_m = \tilde{B}_m = \tilde{C}_m = 0$$

Hence, the Fourier coefficients U_m, V_m, W_m may be determined from a set of equations which do not contain $\tilde{U}_m, \tilde{V}_m, \tilde{W}_m$. This means that the toroid under uniform external pressure can buckle into a mode that is either symmetric or antimetric about line A-A in Figure 1, and these modes can be investigated separately. The symmetric mode is referred to as Mode A and the antimetric mode as Mode B.

The solution of the stability equation will be ou*   d for Mode A (the symmetric mode). The solution for Mode B is similar. The displacement components for Mode A are represented as

$$u_n(\phi) = \sum_{m=1}^{\infty} U_m \sin m\phi \qquad (4a)$$

$$v_n(\phi) = \sum_{m=o}^{\infty} V_m \cos m\phi \qquad (4b)$$

$$w_n(\phi) = \sum_{m=o}^{\infty} W_m \cos m\phi \qquad (4c)$$

Inserting these equations into the stability equation in its differential form results in a set of linear homogeneous algebraic equations similar to equations (3).

$$\sum_{m=1}^{\infty} A_m \sin m\phi = 0 \qquad (5a)$$

$$\sum_{m=o}^{\infty} B_m \cos m\phi = 0 \qquad (5b)$$

43

$$\sum_{m=o}^{\infty} C_m \cos m\phi = 0 \qquad (5c)$$

Since $\sin m\phi$ and $\cos m\phi$ are linearly independent, we must have

$$A_m = 0 \qquad (6a)$$

$$B_m = 0 \qquad (6b)$$

$$C_m = 0 \qquad (6c)$$

By letting $m=1,2,3,\ldots$ in Equations (6), we obtain an infinite system of algebraic equations having the Fourier coefficients U_m, V_m, W_m as the unknowns.

Using matrix notation, Equations (6) are written as

$$[R] \left\{ V \right\} - \omega[S] \left\{ V \right\} = \left\{ 0 \right\} \qquad (7)$$

where $[R]$ and $[S]$ are square coefficient matrices and

$$\left\{ V \right\} = \left\{ \begin{array}{c} U_m \\ V_m \\ W_m \end{array} \right\}$$

and

$$\omega = \frac{1}{\lambda} = \frac{1}{\dfrac{pa}{Eh}}$$

The objective of the stability analysis is to determine the lowest value of λ (the eigenvalue) for which Equation (7) admits a nontrivial solution (the eigenvector). The components of the eigenvector are the Fourier coefficients U_m, V_m, W_m. The displacement functions

$$u_n(\phi) = \sum_{m=1}^{\infty} U_m \sin m\phi$$

44

$$v_n(\phi) = \sum_{m=o}^{\infty} {}' V_m \cos m\phi$$

$$w_n(\phi) = \sum_{m=o}^{\infty} {}' W_m \cos m\phi$$

corresponding to the eigenvalue λ are called the eigenfunctions or mode shapes in the meridional direction.

To obtain a solution for Mode A to a particular problem of known geometry, an initial value of n (number of circumferential waves) is selected. By assigning a value to m, the infinite system of algebraic equations (6) is reduced to a finite set of equations.

A matrix iteration technique is used with the algebraic equations in matrix form, Equation (7), to determine from Rayleigh's quotient the lowest eigenvalue $\bar{\lambda}$ of the finite set of equations. Next, the size of the set of equations is increased by increasing the value of m, and the lowest eigenvalue $\bar{\lambda}$ of the new set of equations is determined as before. This procedure is repeated until the successive values of $\bar{\lambda}$ have converged to a value $\bar{\lambda}_{cr}$. Then by varying n and repeating the iterative process with m, we obtain a set of these values $\bar{\lambda}_{cr}$, one for each n considered. The solution (λ_{cr}) for Mode A is given by the minimum value of $\bar{\lambda}_{cr}$ in this set. The critical buckling pressure for Mode A is

$$p_{cr}^A = \lambda_{cr}\left(\frac{Eh}{a}\right) \tag{8}$$

This solution procedure was programmed by Sobel and Flügge for the IBM 7094 computer.

The solution for the antimetric mode, Mode B, is obtained in a manner similar to that for Mode A. For Mode B, the displacement components are represented as

$$u_n(\phi) = \sum_{m=o}^{\infty} {}' \tilde{U}_m \cos m\phi \tag{9a}$$

45

$$v_n(\phi) = \sum_{m=1}^{\infty} \tilde{V}_m \sin m\phi \qquad (9b)$$

$$w_n(\phi) = \sum_{m=1}^{\infty} \tilde{W}_m \sin m\phi \qquad (9c)$$

The solution procedure is the same as for Mode A. In matrix notation, the stability equation is

$$[\tilde{R}] \left\{\tilde{V}\right\} - \omega[\tilde{S}] \left\{\tilde{V}\right\} = \left\{0\right\} \qquad (10)$$

where $[\tilde{R}]$ and $[\tilde{S}]$ are square coefficient matrices and

$$\left\{\tilde{V}\right\} = \left\{ \begin{matrix} \tilde{U}_m \\ \tilde{V}_m \\ \tilde{W}_m \end{matrix} \right\}$$

The critical buckling pressure for Mode B, P_{cr}^B, is obtained in the manner described for the symmetric mode (Mode A).

The buckling pressure for the toroid under consideration is the lesser of the two buckling pressures P_{cr}^A and P_{cr}^B. The toroid will buckle in the meridional mode (symmetric or antimetric) and in the circumferential mode (n) associated with the buckling pressure.

ANALYSIS OF BUSHNELL

The analysis of Bushnell for the prediction of elastic buckling pressures and natural frequencies of vibration of shells under uniform external pressure is described in detail in Reference 6. A brief description of the analysis will be given here.

The complete analysis is for any shell of revolution with or without stiffeners; however, this description is oriented toward the unstiffened toroid and includes only those parts of the analysis pertinent to this geometry.

46

The analysis utilizes an energy method and the finite difference technique to solve the buckling problem. Prebuckling quantities are determined from linear membrane analysis. There is a nonlinear prebuckling analysis available as part of the analysis, but it was not used for the toroid. The assumptions governing the analysis are:

1) The material is elastic.

2) Normals to the middle surface before deformation remain normal after deformation with no change in length.

3) The structure and loads are axisymmetric, and the prebuckling or prestress deformations are axisymmetric.

4) The prebuckling deflections, while considered finite, are moderate. That is, the square of the meridional rotation can be neglected compared to unity.

The energy method used in the analysis is based on the definition of the Hamiltonian formed from the sum of the potential energy and the kinetic energy of the deformed state of the shell

$$H_n = U_s - T_s + U_c^A + U_c^B \tag{11}$$

where

n is number of circumferential waves,

U_s is shell strain energy,

T_s is shell kinetic energy (this term is zero for the buckling problem),

U_c^A and U_c^B are constraint conditions at the A and B ends of the toroid meridian (see Figure 28).

The Hamiltonian is reduced to an algebraic form by expressing the strain energy and constraint conditions in terms of buckling displacements and their derivatives. The derivatives with respect to the meridional coordinate are simulated by two and three point finite difference formulas. Derivatives with respect to the circumferential coordinate are eliminated because $u=u_n \sin n\theta$, $v=v_n \cos n\theta$, $w=w_n \sin n\theta$. The resulting algebraic form is

$$H_n = [q] \left[[K_1] + [K_2] \right] \{q\} \tag{12}$$

47

where

[q] is vector matrix of dependent variables including displacements and Lagrange multipliers corresponding to the constraint conditions,

$$[q] = \{q\}^T$$

$[K_1]$ is stiffness matrix of the undeformed and unstressed shell,

$[K_2]$ is matrix of prestress terms contributing to the stiffness matrix.

$[K_1]$ and $[K_2]$ are obtained from expressions for strain energy and constraint conditions as will be described.

The integral form of the shell strain energy is written as

$$U_s = \frac{\pi}{2} \int_{\substack{\text{meridional} \\ \text{shell} \\ \text{length}}} \left[[S] \left\{\epsilon\right\} + [\omega] \; [N_0] \left\{\omega\right\} + [d] \; [P] \left\{d\right\} \right] r\,ds \qquad (13)$$

where

[S] is vector matrix of buckling stresses and moment resultants,

[ω] is vector matrix of rotation components,

$[N_0]$ is matrix of prestresses,

[d] is vector matrix of displacement components,

[P] is matrix of pressure loading.

$\left\{\epsilon\right\}$, $\left\{\omega\right\}$, $\left\{d\right\}$ are matrices in terms of geometric variables and displacements obtained by utilizing Novoshilov's strain-displacement and curvature-displacement relations.

In order to use the finite difference technique, nodes or mesh points are located along the shell merdian, and the Hamiltonian is written at each mesh point. Hence, the integral expression for strain energy can be written in finite difference notation as a summation over the mesh points along the meridian. The finite difference representation of the displacements and their derivatives are

$$u = \frac{(u_i + u_{i-1})}{2} \qquad v = \frac{(v_i + v_{i-1})}{2} \qquad w = w_i$$

48

$$\frac{du}{ds} = \frac{(u_i - u_{i-1})}{h} \qquad \frac{dv}{ds} = \frac{(v_i - v_{i-1})}{h} \qquad \frac{dw}{ds} = \frac{(w_{i+1} - w_{i-1})}{2h}$$

$$\frac{d^2w}{ds^2} = \frac{(w_{i+1} - 2w_i + w_{i-1})}{h^2}$$

and the strain energy expression takes the form

$$U_s = \frac{\pi}{2} \sum_{i=1}^{N} r_i \, \Delta s_i [q_i] \, [Z] \, \left\{ q_i \right\} \tag{14}$$

where

r_i is radius at i^{th} mesh point,

Δs_i is weighting factor,

N is number of mesh points.

The constraint conditions U_c^A and U_c^B are the equations of displacement and rotation compatability at the ends of the shell meridian. These equations take the form

$$U_c^{A,B} = \left[\lambda_1^{A,B}, \; \lambda_2^{A,B}, \; \lambda_3^{A,B}, \; \lambda_4^{A,B} \right] \left[K^{A,B} \right] \left[Q_1^{A,B} + \chi_o Q_2^{A,B} \right] \left\{ \begin{array}{c} u^* \\ v^* \\ w^* \\ \chi \end{array} \right\} \tag{15}$$

where

$\lambda_1^{A,B}$, $\lambda_2^{A,B}$, $\lambda_3^{A,B}$, $\lambda_4^{A,B}$ are the Lagrange multipliers associated with constraints on displacements and rotations at the ends of the meridian

u^*, v^*, w^*, χ are displacements and rotation at the ends of the meridian

χ_o is a prebuckling rotation,

$Q_1^{A,B}$ is a transformation matrix,

$Q_2^{A,B}$ is a matrix representing the effect of prebuckling meridional rotation on the transformation,

$K^{A,B}$ is a matrix governing which displacement conditions are satisfied at the ends of the meridian, depending on an element being either 0 or 1.

49

The stiffness matrices $[K_1]$ and $[K_2]$ in the Hamiltonian are written using the expressions for strain energy and constraint conditions.

The buckling pressure is the eigenvalue of the pressure that causes H_n to be an extremum. The eigenvector is the mode shape. The extremum is formed by minimizing H_n with respect to all of the [q] components. This generates a set of linear homogeneous algebraic equations

$$\left[[K_1] + [K_2] \right] \left\{ q \right\} = 0 \tag{16}$$

The lowest eigenvalue satisfying

$$\left[[K_1] + [K_2] \right] = 0 \tag{17}$$

gives the buckling pressure, and the corresponding eigenvector gives the mode shape. To solve for the eigenvalue, the analysis uses a technique of successive approximation similar to that used by Cohen,[19] to converge on a solution.

The analysis was performed using a computer program written by D. Bushnell and currently in use at NSRDC. In using this analysis to calculate the buckling pressures for the toroid models tested, the following boundary conditions were used for buckling displacements and rotations at the ends of the meridian labeled A and B (Figure 28):

Symmetric Mode

n	A end of meridian				B end of meridian			
	u^*	v^*	w^*	χ(rotation)	u^*	v^*	w^*	χ(rotation)
0	0	0	free	0	0	0	free	0
1	0	free	0	0	0	free	free	0
2,3	0	free	free	0	0	free	free	0

Antimetric Mode

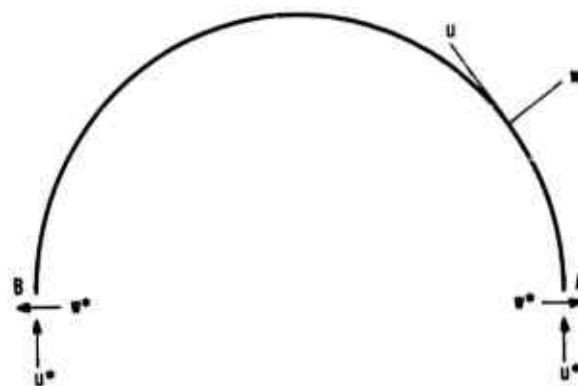| n	A end of meridian				B end of meridian			
	u^*	v^*	w^*	χ(rotation)	u^*	v^*	w^*	χ(rotation)
0	0	0	0	free	free	0	0	free
1	0	0	0	free	free	0	0	free
2,3	free	0	0	free	free	0	0	free

50

Figure 28 - Toroid Meridian used in the
Bushnell Analysis

51

REFERENCES

1. Koiter, W.T., "On the Stability of Torus Shaped Shells," by O. Machnig, Appl. Mech. Reviews, Rev. S670, Vol. 17, p. 786 (Oct 1964).

2. Jordan, P.F., "Vibration and Buckling of Pressurized Torus Shells," AIAA Paper 66-445 (1966).

3. Flügge, W., and Sobel, L.H., "Stability of Shells of Revolution: General Theory and Application to the Torus," Lockheed Missiles and Space Company Report 6-75-6S-12 (Mar 196S).

4. Sobel, L.H., and Flügge, W., "Stability of Toroidal Shells Under Uniform External Pressure," AIAA Journal, Vol. S, No. 3 pp. 42S-431 (Mar 1967).

5. Bushnell, D., "Symmetric and Nonsymmetric Buckling of Finitely Deformed Eccentrically Stiffened Shells of Revolution," AIAA Journal, Vol. 5, No. 8, pp. 14SS-1462 (Aug 1967).

6. Bushnell, D., "Buckling and Vibration of Ring-Stiffened Segmented Shells of Revolution," Lockheed Missiles and Space Company Report 6-78-68-37 (Aug 1968).

7. Healey, John J., "Parametric Study of Unstiffened and Stiffened Prolate Spheroidal Shells Under External Hydrostatic Pressure," David Taylor Model Basin Report 2018 (Aug 196S).

8. Hyman, Barry I., and Healey, John J., "Buckling of Prolate Spheroidal Shells Under Hydrostatic Pressure," AIAA Journal, Vol. 5, No. 8, pp. 1469-1477 (Aug 1967).

9. Flügge, W., "Stresses in Shells," Springer-Verlag, Berlin (1962).

10. Jordan, Peter F., "Stresses and Deformations of the Thin-Walled Pressurized Torus," J. Aero. Sci., Vol. 29, pp. 213-22S (1962).

11. Reissner, Eric, "On Stresses and Deformations in Toroidal Shells of Circular Cross Section which are Acted Upon by Uniform Normal Pressure," Quarterly Appl. Math., Vol. XXI, No. 3, pp. 177-187 (Oct 1963).

S2

12. Sanders, Lyell, J., Jr., and Liepins, Atis A., "Toroidal Membrane Under Internal Pressure," AIAA Journal, Vol. 1, No. 9, pp. 210S-2110 (Sep 1963).

13. Jordan, P.F., "Analytical and Experimental Investigation of Pressurized Toroidal Shells," NASA CR-261 (Jul 1965).

14. Carlson, R.L., et al., "Experimental Studies of Buckling of Complete Spherical Shells," Experimental Mechanics, Vol. 7, No. 7 pp. 281-288 (Jul 1967).

15. Litle, William A., "Reliability of Shell Buckling Predictions," The Massachusetts Institute of Technology Press, Cambridge, Mass. (1964).

16. Hutchinson, John W., "Initial Post-Buckling Behavior of Toroidal Shell Segments," Inter. J. Solids and Structures, Vol. 3, No. 1, pp. 97-115 (Jan 1967).

17. Galletly, G.D. and Reynolds, T.E., "A Simple Extension of Southwell's Method for Determining the Elastic General Instability Pressure of Ring-Stiffened Cylinders Subject to External Hydrostatic Pressure," Proceedings of the Society for Experimental Stress Analysis, Vol. 13, No. 2, pp. 141-152 (1956).

18. Roorda, John, "Some Thoughts on the Southwell Plot," J. Eng. Mech. Div., Proceedings of the Amer. Soc. Civ. Eng., Vol. 6, pp. 37-48 (Dec 1967).

19. Cohen, G.A., "Computer Analysis of Asymmetric Buckling of Ring-Stiffened Orthotropic Shells of Revolution," AIAA Journal, Vol. 6, No. 1, pp. 141-149 (Jan 1968).

DOCUMENT CONTROL DATA - R & D

(Security classification of title, body of abstract and indexing annotation must be entered when the overall report is classified)

1 ORIGINATING ACTIVITY *(Corporate author)*	2a. REPORT SECURITY CLASSIFICATION
Naval Ship Research and Development Center Washington, D.C. 20034	UNCLASSIFIED
	2b. GROUP

3 REPORT TITLE

INVESTIGATION OF ELASTIC STABILITY OF CIRCULAR TOROIDAL SHELLS UNDER UNIFORM
EXTERNAL PRESSURE

4 DESCRIPTIVE NOTES *(Type of report and inclusive dates)*

Final

5 AUTHOR(S) *(First name, middle initial, last name)*

Ely G. Fishlowitz

6 REPORT DATE	7a. TOTAL NO. OF PAGES	7b. NO. OF REFS
May 1970	58	19

8a. CONTRACT OR GRANT NO.	9a. ORIGINATOR'S REPORT NUMBER(S)
S-F 3S.422.303	
b. PROJECT NO	3338
Task 19S6	
c.	9b. OTHER REPORT NO(S) *(Any other numbers that may be assigned this report)*
d.	

10 DISTRIBUTION STATEMENT

This document is subject to special export controls and each transmittal to foreign
governments or foreign nationals may be made only with prior approval of Naval Ship
Research and Development Center, Code 700.

11. SUPPLEMENTARY NOTES	12. SPONSORING MILITARY ACTIVITY
	Naval Ship Systems Command

13 ABSTRACT

A series of eight plastic toroidal shell models of circular
cross section covering a wide geometric range were designed,
built, and tested under uniform external pressure. The results
were compared to collapse pressure predictions of two analyses.
One analysis agreed with experimental collapse pressure to with-
in 10 percent for all but two of the models. The other analysis
agreed with half the models tested to within 10 percent but
seems to be too optimistic for certain geometries. Experimental
strains were recorded and photographs were taken of the models
undergoing deformation during testing. The test results and
analytical predictions indicated that complete toroidal shells
under uniform external pressure appear to be insensitive to im-
perfections.

DD FORM 1473 (PAGE 1)

S/N 0101-807-6801

14 KEY WORDS	LINK A		LINK B		LINK C	
	ROLE	WT	ROLE	WT	ROLE	WT
Toroidal Shells						
Elastic Buckling						
Uniform External Pressure						
Experimental Models						
Undersea Applications						

DD ,FORM,1473 (BACK)

(PAGE 2)